Received: 17 December 2021 | Revised: 24 May 2022 | Accepted: 7 June 2022

DOI: 10.1111/jmg.12686

ORIGINAL ARTICLE

Journal of METAMORPHIC GEOLOGY WILEY

Trace-element heterogeneity in rutile linked to dislocation structures: Implications for Zr-in-rutile geothermometry

Rick Verberne[1,2,3] | **Hugo W. van Schrojenstein Lantman**[4,5] | **Steven M. Reddy**[1,2] | **Matteo Alvaro**[5] | **David Wallis**[6] | **Denis Fougerouse**[1,2] | **Antonio Langone**[7] | **David W. Saxey**[1] | **William D. A. Rickard**[1]

[1]Geoscience Atom Probe Facility, John de Laeter Centre, Curtin University, Perth, Western Australia, Australia

[2]School of Earth and Planetary Sciences, Curtin University, Perth, Western Australia, Australia

[3]Center for Star and Planet Formation, Globe Institute, University of Copenhagen, Copenhagen, Denmark

[4]Department of Geosciences, The Njord Centre, University of Oslo, Oslo, Norway

[5]Department of Earth and Environmental Sciences, University of Pavia, Pavia, Italy

[6]Department of Earth Sciences, University of Cambridge, Cambridge, UK

[7]Institute of Geosciences and Earth Resources, National Research Council (C.N.R), Pavia, Italy

Correspondence
Rick Verberne, Center for Star and Planet Formation, Globe Institute, University of Copenhagen, Øster Voldgade 5–7, Copenhagen DK-1350, Denmark.
Email: rick.verberne@sund.ku.dk

Hugo W. van Schrojenstein Lantman, Department of Geosciences, The Njord Centre, University of Oslo, Oslo.
Email: hwlantman@gmail.com

Handling Editor: Dr. Bernardo Cesare

Present address
Rick Verberne, Center for Star and Planet Formation, Globe Institute, University of Copenhagen, Copenhagen, Denmark

Hugo W. van Schrojenstein Lantman, Department of Geosciences, The Njord Centre, University of Oslo, Oslo, Norway.

Funding information
Australian Research Council, Grant/Award Number: DP210102625; European Research Council, Grant/Award Number: 714936

Abstract

The trace-element composition of rutile is commonly used to constrain *P*–*T*–*t* conditions for a wide range of metamorphic systems. However, recent studies have demonstrated the redistribution of trace elements in rutile via high-diffusivity pathways and dislocation-impurity associations related to the formation and evolution of microstructures. Here, we investigate trace-element migration in low-angle boundaries formed by dislocation creep in rutile within an omphacite vein of the Lago di Cignana unit (Western Alps, Italy). Zr-in-rutile thermometry and inclusions of quartz in rutile and of coesite in omphacite constrain the conditions of rutile deformation to around the prograde boundary from high pressure to ultra-high pressure (~2.7 GPa) at temperatures of 500–565°C. Crystal-plastic deformation of a large rutile grain results in low-angle boundaries that generate a total misorientation of ~25°. Dislocations constituting one of these low-angle boundaries are enriched in common and uncommon trace elements, including Fe and Ca, providing evidence for the diffusion and trapping of trace elements along the dislocation cores. The role of dislocation microstructures as fast-diffusion pathways must be evaluated when applying high-resolution analytical procedures as compositional disturbances might lead to erroneous interpretations for Ca and Fe. In contrast, our results indicate a trapping mechanism for Zr.

KEYWORDS
diffusion, low-angle boundaries, plastic deformation, rutile, trace elements

1 | INTRODUCTION

Rutile is a common accessory mineral formed at middle to lower crustal metamorphic conditions (Dachille et al., 1968) and is stable in ultra-high temperature (UHT) and pressure (UHP) environments (Jamieson & Olinger, 1969; Mei et al., 2014; Withers et al., 2003). The trace-element and isotopic compositions of rutile are routinely analysed to constrain the timing and conditions of geological events. Two of the most important applications of rutile compositional data are U–Pb geochronology (Mezger et al., 1989; Zack, von Eynatten, & Kronz, 2004) and Zr-in-rutile thermometry (Kohn, 2020; Zack, Moraes, & Kronz, 2004). These applications are a significant addition to the traditional options for geothermobarometry and geochronology in the often-restrictive mineral assemblages of UHP metamorphic rocks (Cutts & Smit, 2018; DesOrmeau et al., 2017; Gao et al., 2014; Zack & Luvizottow, 2006). Furthermore, rutile can retain information about the *P*–*T*–*t*-path by preserving mineral and fluid inclusions (Hart et al., 2016, 2018; Ni et al., 2008).

The use of rutile is underpinned by the assumptions that element mobility during geological events subsequent to initial equilibration is well understood and inclusions remain shielded from chemical interaction with the exterior of the host grain. However, many studies have reported disturbances in trace-element distribution and isotopic compositions (Kohn, 2020; Kooijman et al., 2010; Smye & Stockli, 2014; Zhou et al., 2020). These effects have generally been attributed to trace-element migration via volume diffusion. More recently, the presence of twin boundaries, low-angle boundaries (LABs, i.e., subgrain boundaries) and high-angle grain boundaries have been proposed to affect the distribution and mobility of trace elements in natural rutile (Moore et al., 2020; Zack & Kooijman, 2017). Volume diffusion in larger rutile grains is ineffective at temperatures below approximately 600°C for Pb and 650°C for Zr (Cherniak, 2000; Cherniak et al., 2007). However, grain boundaries form fast pathways for intergranular diffusion (Klinger & Rabkin, 1999), particularly in the presence of a fluid.

Rates of intragranular diffusion can be enhanced beyond those of volume diffusion through the presence of intragranular microstructures that contribute to dislocation-impurity pair migration (Imai & Sumino, 1983; Petukhov & Klyuchnik, 2012) and high-diffusivity pathways (Love, 1964; Sutton et al., 1995). Trace-element migration by dislocation-impurity associations relies on the coupled migration of dislocations and trace elements trapped in and around them. This mechanism can lead to the removal of trace elements into the grain-boundary network (Imai & Sumino, 1983; Petukhov & Klyuchnik, 2012). Alternatively, the increasing concentration of solutes can immobilize the migrating dislocation leading to a localized trace-element enrichment (Cottrell & Bilby, 1949; Dubosq et al., 2019; Imai & Sumino, 1983; Petukhov & Klyuchnik, 2012). High-diffusivity pathways can form along microstructures related to growth and deformation, such as dislocations, low- and high-angle boundaries or twin boundaries (Fougerouse, Reddy, et al., 2021; Keller et al., 2006; Love, 1964; Lund et al., 2006; Plümper et al., 2012; Reddy et al., 2007; Timms et al., 2006; Verberne et al., 2022; Vukmanovic et al., 2014).

Identifying these effects in geological materials has remained challenging due to limitations in the spatial resolutions of techniques capable of measuring chemical and isotopic composition (Reddy et al., 2006; Timms et al., 2006; Timms et al., 2011). Advances in analytical techniques allow for correlation among high-spatial resolution chemical and isotopic data with microscale and nanoscale structures. Atom probe tomography (APT) is one such technique with high spatial resolution providing chemical and isotopic information in three dimensions (Gault et al., 2012; Larson et al., 2013). Over the last 5 years, this technique has proven to be a powerful tool within the field of Earth sciences (Reddy et al., 2020; Saxey et al., 2018). The combination of APT with analytical techniques employing larger spot sizes (e.g., LA-ICP-MS or SIMS) allows for the correlation of geochronological data (Peterman et al., 2016; Peterman et al., 2019; Seydoux-Guillaume et al., 2019; Valley et al., 2014, 2015; Verberne et al., 2020). Furthermore, APT can reveal a structure-chemistry relationship down to the nanoscale when applied in combination with high-resolution structural imaging techniques, such as electron backscatter diffraction (EBSD), transmission Kikuchi diffraction (TKD) or transmission electron microscopy (TEM) (Fougerouse et al., 2018; Fougerouse et al., 2019; Fougerouse, Reddy, et al., 2021; Kirkland et al., 2018; Montalvo et al., 2019; Piazolo et al., 2016; Reddy et al., 2016, 2020; Verberne et al., 2022).

This contribution investigates the characteristics and underlying processes of trace-element heterogeneities associated with dislocation structures in low-angle boundaries related to crystal-plastic deformation of rutile. The rutile is located within deformed omphacite veins from the UHP-low-temperature (LT) metamorphic Lago di Cignana unit (LCU), Italy. The LCU provides an excellent opportunity for studying the effect of diffusion along dislocations. The minerals were strained during HP deformation resulting in dislocation microstructures, while the low temperatures ensured that volume diffusion was ineffective and thus did not obscure the effect of

dislocations. By the combination of a range of analytical techniques, the study first constrains the growth and deformation history of rutile in relation to *P–T* conditions. Then, microscale and nanoscale analytical techniques are applied to investigate the relation between the plastic deformation of rutile and the segregation of trace elements. The results highlight the complexity that can arise from the interplay between different structural features and how these structures correlate with nanoscale chemical heterogeneities.

2 | GEOLOGICAL SETTING

2.1 | Geological overview

The Lago di Cignana unit is a lens of UHP metabasic and metasedimentary rocks within the Zermatt-Saas unit (ZSU), an ophiolitic unit of generally high-pressure metamorphic grade (Figure 1). The ZSU was subducted and underwent eclogite-facies metamorphism during the Alpine orogeny (Rubatto et al., 1998), reaching peak metamorphic conditions of 600–630°C, 2.7–2.9 GPa determined for metasediments (Reinecke, 1998) and 590–605°C, >3.2 GPa based on eclogites (Groppo et al., 2009). Subsequently, the LCU was exhumed and juxtaposed with the overlying lower-grade (greenschist–amphibolite facies) Combin zone (Figure 1) (Amato et al., 1999; Kirst & Leiss, 2017; Reddy et al., 2003). As one of few exposed ophiolitic units exhumed after Alpine UHP metamorphism, the LCU is a key locality for insight into fluid–rock interaction at great depth in subduction zones (Frezzotti et al., 2011; Halama et al., 2020; van Schrojenstein Lantman et al., 2021).

The LCU has been the subject of numerous geochronological studies aimed at pinpointing the timing of formation and subduction of the Piemonte-Ligurian oceanic crust. Prograde to peak metamorphic ages have been previously determined as 48.8 ± 2.1 Ma (Lu-Hf garnet-omphacite-whole rock, Lapen et al., 2003), 44.1 ± 0.7 Ma (U/Pb zircon mean age, Rubatto et al., 1998) and 40.6 ± 2.6 Ma (Sm-Nd garnet-whole rock, Amato et al., 1999). Early exhumation of the LCU or ZSU as a whole is dated as 41.6 ± 0.2 and 39.8 ± 0.2 Ma (Rb-Sr phengite-clinozoisite, Skora et al., 2015), 41–39 Ma (K-Ar white mica range of ages, Gouzu et al., 2016), 38 ± 2 Ma (Rb-Sr phengite-whole rock, Amato et al., 1999) and 45–36 (Rb-Sr various minerals, range of ages, Reddy et al., 1999). Rb-Sr white-mica ages of 39–36 Ma for the Combin Fault represent the exhumation leading to the emplacement of the ZSU below the Combin Zone, in agreement with rapid exhumation after peak metamorphism (Kirst & Leiss, 2017; Reddy et al., 1999, 2003).

2.2 | LCU eclogite

The main lithologies of the LCU are quartzite and schist locally bearing garnetite lenses, calc-schist, marble and eclogite (Forster et al., 2004). Garnet- and glaucophane-rich zones in the eclogite may reflect compositional differences due to fluid–rock interaction (van Schrojenstein Lantman et al., 2021) or related to pillow basalts (van der Klauw et al., 1997). The peak metamorphic assemblage consists of garnet, omphacite, glaucophane, lawsonite, phengite, rutile, and minor coesite and zircon. The latter two minerals are also present as inclusions in omphacite and garnet (Groppo et al., 2009; King et al., 2004). Lawsonite has broken down to pseudomorphs of epidote and paragonite. Titanite, ilmenite, Ca-amphibole and biotite preserved as inclusions in garnet cores represent an early prograde metamorphic mineral assemblage. The eclogite is rich in TiO_2 (>2 wt.%), resulting in an abundance of rutile (Groppo et al., 2009). A multitude of veins has been identified in the LCU eclogites, mainly consisting of

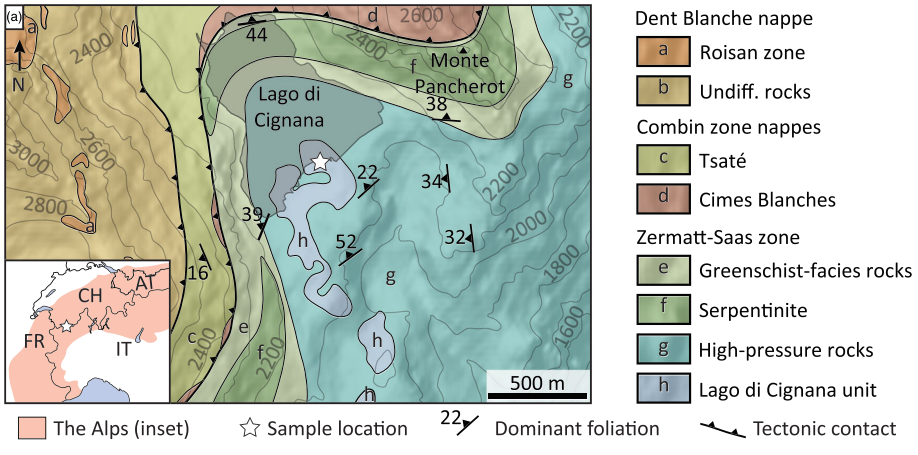

FIGURE 1 Simplified geological map of the sample area around Lago di Cignana, modified after Kirst and Leiss (2017) and references therein. AT, Austria; CH, Switzerland; FR, France; IT, Italy [Colour figure can be viewed at wileyonlinelibrary.com]

omphacite, glaucophane, quartz (potentially after coesite), epidote/clinozoisite and retrogressed lawsonite. The relative timings of vein formation range from UHP metamorphism to retrograde metamorphic stages during exhumation.

The deformation of the LCU eclogites has been established in detail. Müller and Compagnoni (2009) indicate that pyroxene is pervasively deformed by dislocation creep with dynamic recrystallization resulting from grain-boundary migration. At the onset of extension, the deformation became localized, leading to the formation of shear bands (van der Klauw et al., 1997). Little to no deformation took place in the eclogites during the first 40 km of exhumation, down to *P–T* conditions of <1.5 GPa, 500–550°C (van der Klauw et al., 1997). Following this part of the exhumation, further deformation within eclogites was associated with a retrograde mineral assemblage of hornblende, albite and epidote (Kirst & Leiss, 2017).

3 | METHODS

This contribution is a collaboration between the Geoscience Atom Probe group of Curtin University and the University of Pavia, where measurements were performed concurrently. To ensure that the data obtained represent equivalent material, two near-identical thick sections of 100 μm thickness were prepared from the same chip of the hand specimen (Figure 2b). Work conducted at the University of Pavia focused on multiple grains of a variety of minerals with data acquisition at scales of 1–50 μm, while the complementary work at Curtin University focused on the microscale and nanoscale characterization of a single large rutile crystal (Grain ID - Rt-1, Figures 2b and 3a).

3.1 | Raman spectroscopy

Raman spectroscopy for the purpose of the identification of mineral inclusions was conducted at the University of Pavia using a Horiba LabRam HR Evolution spectrometer with a holographic grating of 1,800 grooves/mm. The Horiba is equipped with an Olympus BX41 confocal microscope and operated at a constant temperature of 20 ± 1°C. Raman spectra were excited using the 514.532 nm line of a solid-state (YAG) laser. The laser power on the sample surface was approximately 1–2 mW.

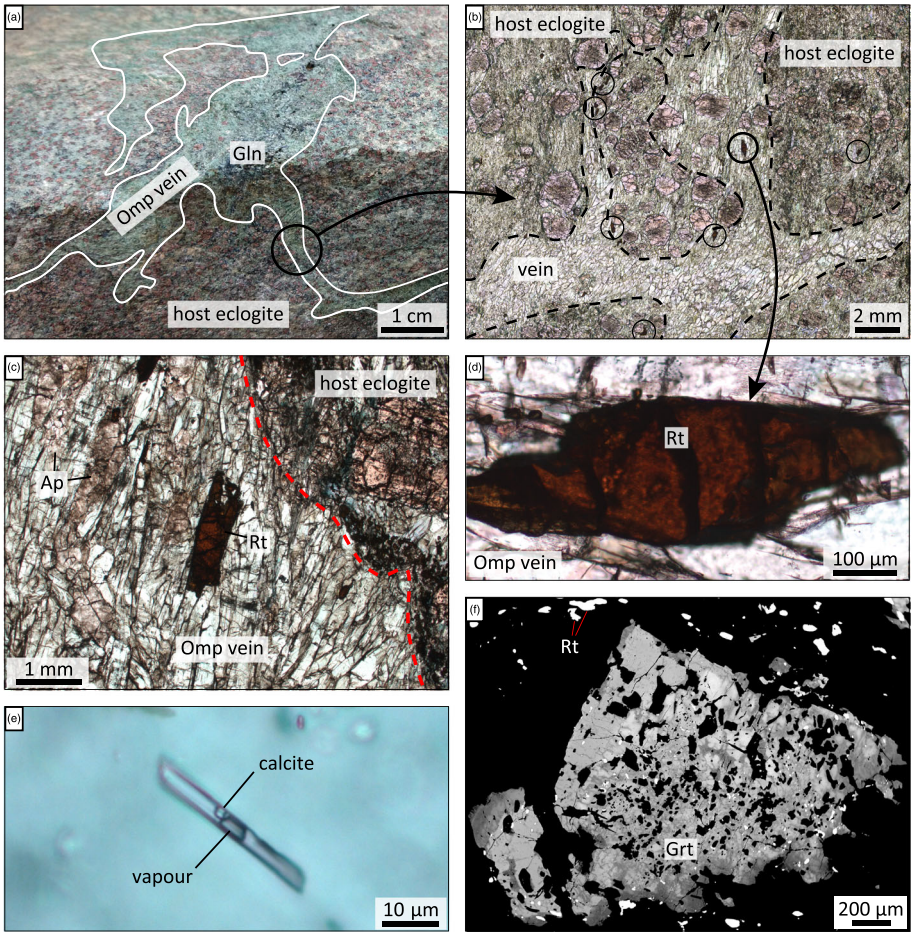

FIGURE 2 (a) Outcrop photograph of eclogite containing an omphacite-glaucophane vein. (b–e) Optical micrographs of analysed thick sections. (b) Scan of a thick section that includes both omphacite vein and host eclogite. The boundary between the two is marked by the dashed black lines. Circles indicate the location of several large grains of rutile. The marked grain with the arrow leading to (d) is the grain selected at nanoscale analyses at Curtin University, Rt-1 (see Figure 3). (c) Close-up of a large rutile grain and the contact between the omphacite vein and the host eclogite, marked by the red dashed line. (d) Close-up of the rutile grain selected for nanoscale analyses. (e) A fluid inclusion in omphacite in the vein, containing a vapour bobble and a daughter crystal of calcite as identified with Raman spectroscopy. (f) BSE image of garnet in the host eclogite directly adjacent to the omphacite vein. Mineral abbreviations are from Whitney and Evans (2010). [Colour figure can be viewed at wileyonlinelibrary.com]

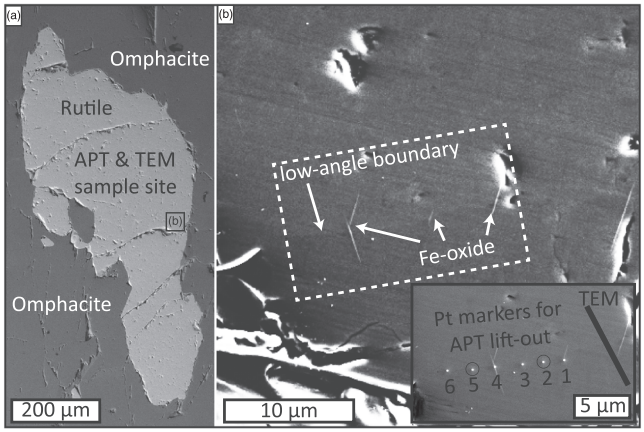

FIGURE 3 (a) Backscatter electron image of the rutile grain Rt-1 highlighting the APT and TEM lift-out area and demonstrating that the rutile grain is completely surrounded by omphacite. (b) Close-up secondary electron image of the lift-out site. The low-angle boundary is made visible via the electron channelling effect. Fe-oxide exsolutions clearly intersect this boundary. The inset shows the deposited Pt-buttons that assist during preparation of the APT specimen. The encircled markers correspond with the two APT analyses that contain the LAB within the analytical volume. The TEM section was taken to the right-hand side of APT spec. 1.

The spectrometer was calibrated by matching the Raman spectrum to the silicon peak at 520.5 cm^{-1}.

3.2 | LA-ICP-MS and Zr-in-rutile geothermometry

The trace-element composition of rutile was determined by laser ablation inductively coupled plasma mass spectrometry (LA-ICP-MS) at the Istituto di Geoscienze e Georisorse of the National Research Council in Pavia. The instrument couples an Excimer Laser 193 nm ArF (GeoLas200 Microlas) with a Triple Quadrupole (8900 QQQ from Agilent). Elements that were measured are ^{7}Li, ^{9}Be, ^{11}B, ^{23}Na, ^{25}Mg, ^{27}Al, ^{29}Si, ^{39}K, ^{43}Ca, ^{44}Ca, ^{45}Sc, ^{47}Ti, ^{51}V, ^{53}Cr, ^{55}Mn, ^{57}Fe, ^{59}Co, ^{60}Ni, ^{63}Cu, ^{66}Zn, ^{75}As, ^{85}Rb, ^{88}Sr, ^{89}Y, ^{90}Zr, ^{93}Nb, ^{95}Mo, ^{118}Sn, ^{121}Sb, ^{133}Cs, ^{138}Ba, ^{139}La, ^{140}Ce, ^{141}Pr, ^{146}Nd, ^{149}Sm, ^{151}Eu, ^{157}Gd, ^{159}Tb, ^{163}Dy, ^{165}Ho, ^{167}Er, ^{169}Tm, ^{173}Yb, ^{175}Lu, ^{177}Hf, ^{181}Ta, ^{182}W, ^{208}Pb, ^{232}Th and ^{238}U. NIST-SRM610 was used as an external standard, whereas Ti was adopted as an internal standard for rutile. In each analytical run, the USGS reference samples BCR2 and NIST612 (Norman et al., 1996; Pearce et al., 1997; Rocholl et al., 1997) were analysed together with the unknowns for quality control. Precision and accuracy are better than 5% and 10%, respectively. Data reduction was performed using the Glitter software package (van Actherbergh, 2001). A laser beam, 50 µm in diameter, was employed to analyse 16 spots across six rutile grains, measuring core and rim separately when grain size allowed and using an average TiO_2 content of 99 wt.% as an internal standard.

The concentration of Zr in rutile grown in equilibrium with zircon and quartz/coesite provides temperature estimates that accurately reflect crystallization temperature (Zack, von Eynatten, & Kronz, 2004). Accurate results from Zr-in-rutile geothermometry require constraints on the activities of Zr (a_{Zr}) and Si (a_{Si}) (Kohn, 2020; Tomkins et al., 2007; Watson et al., 2006; Zack, Moraes, & Kronz, 2004). In cases where a_{Si} and/or $a_{Zr} < 1$, the Zr-in-rutile geothermometer will provide overestimate or underestimate of the temperature, respectively. It is assumed that $a_{Si} = a_{Zr} = 1$ if Zr- and Si-bearing phases (e.g., zircon and quartz) were in equilibrium with rutile (Zack, Moraes, & Kronz, 2004). Zr-in-rutile thermometry was applied using the *P*-sensitive 'combined' calibration by Kohn (2020).

3.3 | Scanning electron microscopy

Rutile was characterized by using the TESCAN MIRA3 field-emission scanning electron microscope at the John de Laeter Centre (JdLC), Curtin University, Perth, Australia. BSE images were collected at a working distance of 15 mm and an accelerating voltage of 20 kV. For combined electron backscatter diffraction (EBSD) and energy dispersive X-ray spectroscopy (EDS) imaging, the SEM was operated at a working distance of 15 mm with the stage tilted to 70°, and an accelerating voltage of 20 kV was applied. EBSD data were acquired at a step size of 1 µm, and the match units for rutile (Swope et al., 1995) and omphacite (Oberti & Caporuscio, 1991) were obtained from the American Mineralogist crystallography database (801448-45x).

Transmission Kikuchi Diffraction (TKD) was performed on the APT specimens to assist with targeting the LABs during sample preparation for APT and to provide correlation with APT data. TKD was performed with a step size of 15 nm and at a working distance of 9 mm, 90° tilt and an accelerating voltage of 30 kV.

Post-processing of EBSD and TKD data was performed in Matlab®, version R2020b, using the free toolbox MTEX Version 5.3 (Bachmann et al., 2010). Images were plotted using the 'roma' scientific colour map of Crameri (2018). Post-processing involved a noise-reduction procedure by removal of groups of <5 adjacent pixels ('Wild' spikes/shards) with crystal orientations within 10° of those of their neighbours. The procedure was followed by applying a 5 × 5 pixel median filter. The filter smooths the orientations in the EBSD data while preserving subgrain boundaries (see Data S1, DR-1).

3.4 | Focussed-ion-beam SEM

Specimen preparation for TEM and APT was conducted on the Tescan Lyra Ga^+ Focused Ion Beam Scanning Electron Microscope (FIB-SEM) (Figure 3), within the JdLC. The FIB-SEM was operated at an accelerating voltage of 30 kV. TEM and APT specimens were extracted from one low-angle boundary in a single grain. The TEM foil was mounted on a copper half-grid and thinned to <100 nm followed by a 2 kV cleaning routine to remove damage induced by 30 kV specimen preparation. APT specimens were precisely targeted using electron-beam deposited markers and followed by the standard lift-out and sharpening procedures and 2 kV clean-up routine (Rickard et al., 2020). TKD imaging ensured that the LAB was present close to the apex of the tip after final sample preparation and consequently within the field-of-view for APT analysis. Final secondary-electron (SE) imaging was performed in SEM-mode only at a working distance of 6 mm and an accelerating voltage of 10 kV.

3.5 | Transmission electron microscopy

TEM analysis was performed on the FEI Talos FS200X Field Emission Gun TEM equipped with a Super-X EDS detector housed in the JdLC, Curtin University, Australia. The TEM was operated at 200 kV. TEM imaging was conducted in both bright- and dark-field (BF and DF) modes. The TEM diffraction investigation was conducted with the assistance of Kikuchi patterns that were generated by convergent beam electron diffraction (CBED). A small spot was used to minimize the beam-related damage to the sample, and the sample was tilted to align a zone axis or meet a two-beam condition to acquire selected-area diffraction (SAD) patterns. Both BF and DF TEM imaging was undertaken with the objective apertures after tilting the sample to a diffraction condition within 20°.

Chemical analysis was conducted using the attached two pairs of Super-X detectors. The TEM is fitted with four scanning transmission electron microscopy (STEM) detection systems: high-angle annular dark-field (HAADF), upper dark-field (DF4), lower dark-field (DF2) and bright-field (BF). The contrast in HAADF images results predominantly from chemical/phase differences, and the contrast in BF images results predominantly from orientation differences. The DF4 and DF2 detectors reveal both chemical and orientation contrasts at different angles. TEM, STEM and EDS data acquisition was conducted with the Velox software.

3.6 | Atom probe tomography

APT analyses were performed on a Cameca Local Electrode Atom Probe (LEAP) 4000X HR at the Geoscience Atom Probe Facility, Curtin University. The LEAP was operated in laser-assisted mode at a pulse rate of 200 kHz, a laser pulse energy of 50 pJ, a base temperature of 50 K and a detection rate of 0.8% (1,600 ions s^{-1}) based on recommendations by Verberne et al. (2019). Five needle-shaped specimens were run in the atom probe yielding 38×10^6–95×10^6 ion counts. All specimens remained intact after the run. Post-processing was performed using Cameca's Integrated Visualization and Analysis Software (IVAS) 3.8.0., using a field of 26 V/nm following recommendations in Fougerouse, Saxey, et al. (2021). Peaks in the mass spectra were labelled per individual element for specific ionization states and ranged with a constant width of 0.2 Da unless clearly resulting in the measurement of background signals. Detailed information about acquisition and post-processing is provided in Data S2 (DR-2) based on Blum et al. (2018). For visualization and compositional analyses, isoconcentration surfaces were computed in 3D using IVAS, with error bars on the proximity histograms are given as 1σ (Hellman et al., 2000). Whereas 1D concentration profiles provide insight into the distribution of elements across individual features, proximity histograms (Hellman et al., 2000) are ideal to visualize the overall extent of trace-element enrichment for a selected feature, as well as providing better statistical insights due to measuring significantly larger volumes. Proximity histograms are measured orthogonal to each point on an isoconcentration surface. The distance is based on the smallest radius of all included features (5 nm). Proximity histograms are based on a 0.8 at. % Fe isoconcentration surface.

4 | RESULTS

4.1 | Sample characterization

The studied sample, obtained at grid reference 45°52′42.5″N 7°35′33.3″E (Figure 1), is an eclogite cross-cut by a network of omphacite veins up to approximately 1 cm in width (Figure 2a–c). In the outcrop, the vein network appears undeformed to weakly deformed (Figure 2a). Besides omphacite as the main component, the veins also contain rutile, apatite and minor glaucophane (Figure 2). The host eclogite consists mostly of garnet, omphacite of a smaller grain size than in the vein, glaucophane and abundant rutile grains. Rutile is commonly concentrated at the contact between the host eclogite and the vein (Figure 2b,c). Locally, the distinction

between the vein and wall rock is less clear, potentially due to the presence of wall rock-derived grains, such as garnet and rutile, within the vein (Figure 2b). Most crystals in the vein are up to 1 mm in length and exhibit a shape preferred orientation (sub-vertical in Figure 2c). In contrast, glaucophane rarely exceeds a grain size of 100 μm. Rutile within the wall rock occurs as grains smaller than 100 μm, which is significantly smaller than rutile in the veins. No deformation features in the vein are visible in the hand specimen or thick section. Primary fluid inclusions with vapour bubble and calcite daughter crystal, as identified with Raman spectroscopy, are locally present within omphacite in the vein (Figure 2e). Garnet in the host eclogite exhibits erratic compositional zonation, as visualized by BSE imaging (Figure 2f).

4.2 | Inclusion characterization

Coesite, apatite and zircon are identified within omphacite by Raman spectroscopy, the latter mineral inclusion being the most abundant (Figure 4a,b,d). Calcite is also present, although only as daughter crystals in primary fluid inclusions. Zircon, omphacite and rutile were identified as inclusions in garnet. Inclusions hosted in rutile are difficult to identify due to the strong Raman signal of rutile. Nevertheless, quartz inclusions were identified in rutile (Figure 4c,e). No radial fractures were observed around these inclusions. Ubiquitous exsolution platelets in rutile (Figure 4c) could not be identified using Raman spectroscopy.

4.3 | Rutile geochemistry

Figure 5a presents the range of concentrations of all elements in the rutile that consistently yielded concentrations above the detection limit. The full dataset is available in Data S3 (DR-3), and locations of analysed rutile grains are given in Figure S1 (DR-7). Measured Zr concentrations in rutile are in the range 31.5–52.6 ppm, taking into account the 1σ uncertainty (Figure 5b). Most rutile cores contain higher Zr concentrations than their respective rims, and overall differences in Zr concentration exist between grains beyond the uncertainty of the measurements. As a result, the Zr-in-rutile thermometry does not result and reflect a single temperature. Using the full range of Zr concentrations including analytical

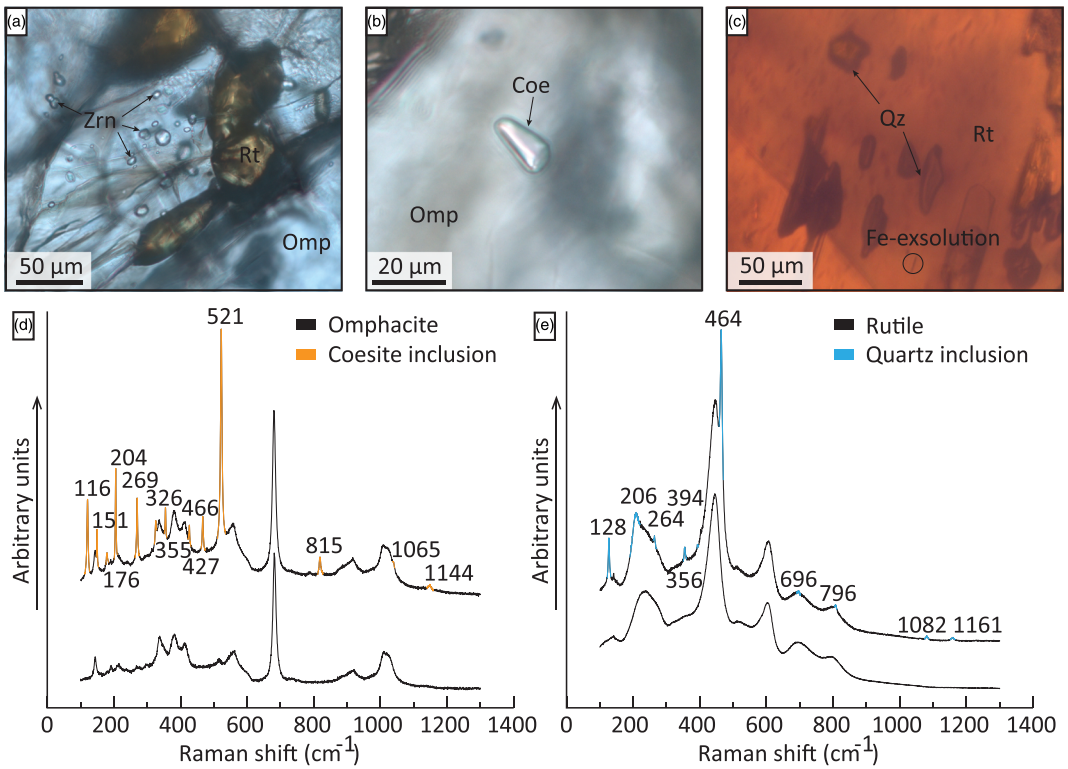

FIGURE 4 (a–c) Micrographs taken with plane-polarized light revealing (a) the presence of zircon (Zrn) inclusion in omphacite (Omp), (b) a coesite (Coe) inclusion in omphacite and (c) quartz (Qz) and Fe-rich inclusions in rutile (Rt). Scale bars indicate 50 μm. (d, e) Representative Raman spectra demonstrating the presence of a coesite inclusion in omphacite (d) and a quartz inclusion in rutile (e) [Colour figure can be viewed at wileyonlinelibrary.com]

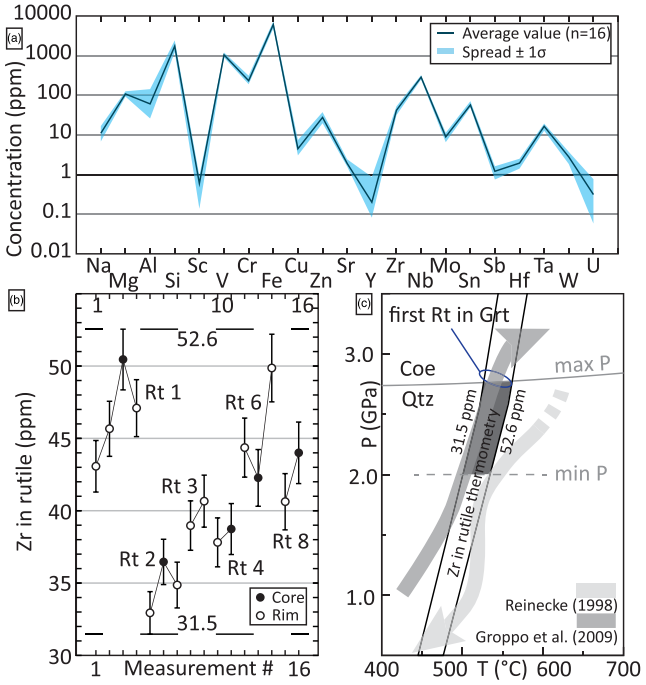

FIGURE 5 (a) Elemental concentrations measured by LA-ICP-MS, with the average shown as a solid line. (b) All measured concentrations of Zr in rutile, with error bars representing 2σ. Dashed horizontal lines indicate the full possible range of Zr concentrations based on these analyses. (c) P–T–t diagram illustrating the metamorphic history, including the Zr concentrations in rutile and the corresponding temperature values using Zr-in-rutile geothermometry. 'First Rt in Grt' indicates the approximate first occurrence of Rt inclusions in garnet, marked in P–T space according to Groppo et al. (2009). [Colour figure can be viewed at wileyonlinelibrary.com]

uncertainty, and a pressure range from 2.0 GPa (lower-*P* estimate for the first appearance of rutile, after Groppo et al., 2009) up to the quartz-coesite transition at 2.7–2.8 GPa, Zr-in-rutile thermometry results in a range of 500–565°C (Figure 5b). Propagated temperature uncertainties using the applied combined calibration are on the order of 10–15°C (Kohn, 2020).

4.4 | Microstructural analysis

The various substructures within the rutile are characterized by different analytical techniques. The BSE images presented in Figure 3b reveal a LAB evident as subtle orientation contrast and show the presence of Fe-rich exsolution platelets crosscutting the LAB. These thin, Fe-rich platelets are visible throughout the entire grain, both in contact with LABs and isolated from them. The angles are systematic within a grain. Measured at one location, the apparent angles are acute, 35° between two platelets, and intersecting the LAB at apparent angles of 69° and 78° in Figure 3b.

The EBSD maps reveal that rutile, present within the omphacite vein, is deformed (Figure 6a).

This deformation is expressed in the form of LABs with misorientation angles of up to approximately 2° across individual boundaries (Figure 6b) resulting in a total misorientation of approximately 25° across the grain (Figure 6c). The EBSD maps of the whole grain show that the LAB traces change in orientation, with the dominant orientation being subhorizontal (100–280°) and parallel to [100] (Figure 6c,d) and with the misorientation axis being <010> at our region of interest (Figure 6c,d). However, the misorientation axes also have a second preferred orientation centred on <110> (Figure 6c,d), resulting in crystal directions, such as [100], exhibiting spreads of about ∼19° in the longitudinal direction and ∼9° in the latitudinal direction. These complex misorientation characteristics indicate the operation of multiple slip systems.

TKD maps of the APT specimens revealed that two specimens contain LABs that were originally close-to perpendicular to the surface of the thin section (Figure 7). The two specimens come from the same crystal approximately 5 μm apart, yet the boundary observed within the specimens dips in opposite directions. The geometry of these low angle boundaries and the misorientation and dispersion axes close to being parallel with [110] for M2 and parallel to [010] M5 suggest the active slip system to be {110}[001] (M2) and {010}[001] (M5).

4.5 | Nanoscale structure and composition

The TEM foil HAADF and dark-field images indicate that the LAB is composed of approximately parallel dislocations aligned along the boundaries (Figure 8b,c). The separation of dislocations varies in the range 5–35 nm (Figure 8c,d). The LABs are not planar but instead exhibit an irregular pattern and are offset by steps approximately 10 nm in height (Figure 8b, white arrow).

As expected from the APT TKD maps, two of the five analysed specimens contained a LAB within the field of view.

The 3D reconstructions of M2 (Figure 9a) and M5 (Figure 9d) reveal the presence of a mix of chemically distinct linear features that intersect. These are highlighted by contrasting distributions of Fe (red) and Ca (purple) and are visualized using Fe isoconcentration surfaces (0.8 at. % Fe) in Figure 9, overlain with the Ca distribution. For a 3D representation of the data, see Videos S1 and S2 and and Data S4. Note that D images of 3D features sometimes create false angles.

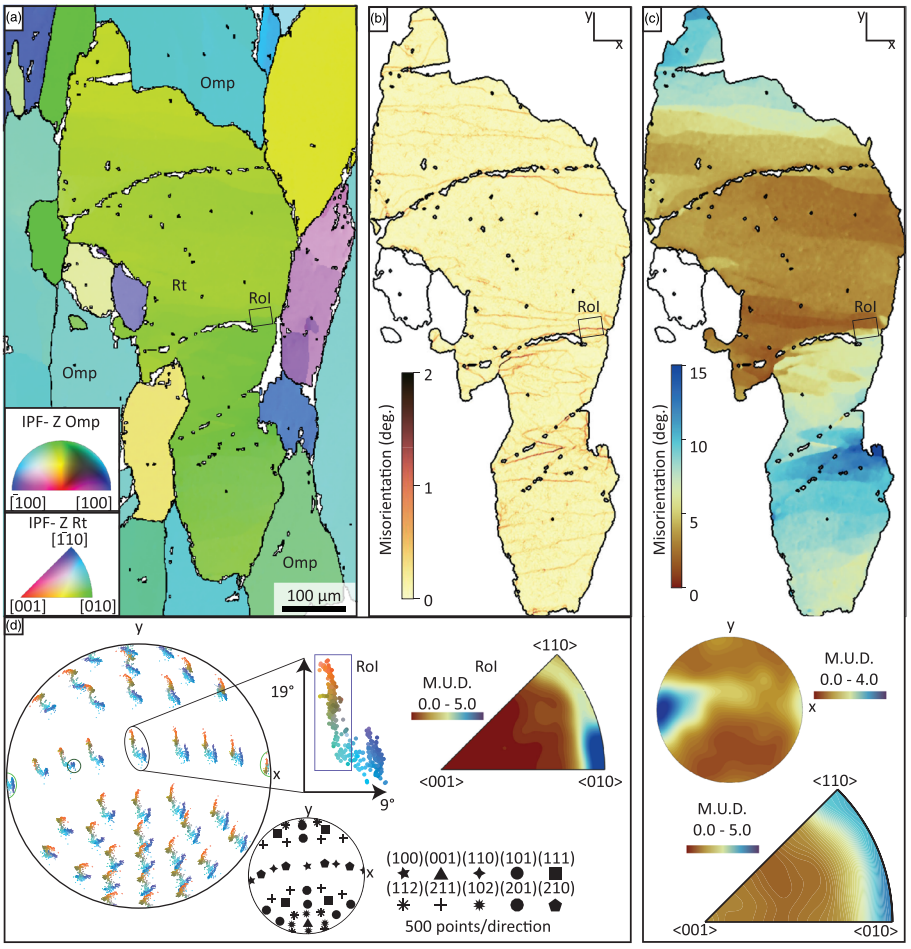

FIGURE 6 (a–c) EBSD maps of the rutile grain of interest with the *Z* axis of the map defined as normal to the page. The box marked RoI indicates the APT lift-out area. (a) Crystal orientation represented by the crystallographic direction aligned with the *Z* axis of the map. (b) Local-misorientation map revealing the presence of low-angle boundaries. (c) Map of misorientation with respect to the mean orientation of the grain. The misorientation pole figure presents the misorientation axes of LABs in the specimen reference frame, whereas the misorientation inverse pole figure presents the same axes in the crystal reference frame. (d) Pole figure with colours based on (c). The light- and dark-green circles indicate that the dispersion of crystal directions occurs about axes centred on [100]/[010] and [110], respectively. Five-hundred points per plotted direction are shown. The misorientation pole figure presents the misorientation axes of the LAB within the RoI selected for the APT lift-out. [Colour figure can be viewed at wileyonlinelibrary.com]

APT chemical analysis of the rutile matrix demonstrates a homogeneous distribution of trace elements outside the LAB, with a TiO_2 concentration of approximately 96 at. % and H concentration of 2–3 at. % (1, 2 and 3 Da) (Figure 10). Pb is only observed above the background as $^{208}Pb^{++}$ (104 Da) and is distributed homogeneously.

Chemical heterogeneities are only observed in relation to the LAB in M2 and M5 and not in the rutile matrix. Sub-horizontal, parallel linear features parallel to <100> are present in both specimens. As <100> is also the most common misorientation axis (Figure 6), these features are interpreted as edge dislocations (Figure 9). The dislocations within a single specimen all lie in the same plane with spacings of approximately 10 nm. In both specimens, the dislocations are enriched in trace elements (Data S4, DR-6), compensated by reductions in Ti concentration (Figures 9 and 10). The differences in H concentration are due to the OH-species, mainly OH^+ (17 Da), while H-species at 1, 2 and 3 Da in the mass spectrum remain homogeneous (Data S4, DR-6). The concentrations are evaluated using 1D concentration profiles (Figure 10). These profiles exhibit Fe concentrations reaching 1 at. % in the LAB. Al, Si and Ca concentrations are also higher in the LAB than in the matrix at <0.05–0.25 at. %, 0.15 at. % and 0.1 at. %, respectively, across individual structures.

Approximately every 50 nm, the plane in which the dislocations lie is offset by roughly 10 nm (Figure 9c). These 'steps' still exhibit the dislocation pattern within their substructure (Figure 9c). The dislocations have higher concentrations of trace elements compared to the matrix. The chemical composition of these steps is displayed as a 1D concentration profile (Figure 10). Similar to the dislocations outside the steps, those inside the steps are associated with elevated concentrations of Fe (0.5–4.2 at. %), Al (<0.05–0.45 at. %) and Si (<0.05–0.1 at. %) relative to the concentrations in the matrix. In addition, Zr concentrations in the dislocations are 0.1 at. %, up from <0.05 at. % in the matrix and other dislocations outside the steps. The Ca signal in this feature is notably low at <0.05 at. %.

Extending from the dislocations in M5 are two near-vertical Fe-enriched features that we will refer to as platelets (Figure 9b). The acute angle between these two platelets is 59° (Figure 9f). The platelets intersect the LAB at

60° and 61°. The chemistry of these platelets is comparable to the chemistry of the steps, but the degree of enrichment of Fe is less, and Ca and Si are absent. Fe reaches concentrations of 2 at. % (up from 0.5 at. % in the matrix), and H increases from approximately 2 at. % to 3.5 at. %. The concentration of Zr within the 1D profile is 0.06 at. %, and the concentration of Al is 0.12 at. %.

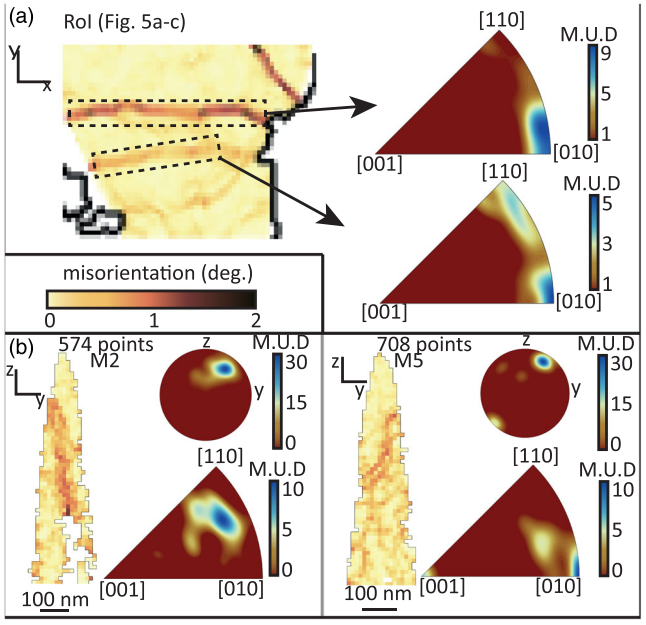

FIGURE 7 (a) EBSD local-misorientation map of the RoI in Figure 5. Misorientation inverse pole figures of two boundaries in the RoI are shown. (b) TKD local-misorientation maps of misorientation pole figures and misorientation inverse pole figures of APT needles M2 and M5 extracted from the lower LAB in the RoI in (a). Respectively, 574 and 708 have been plotted for M2 and M5. [Colour figure can be viewed at wileyonlinelibrary.com]

Two entangled, sub-vertical dislocations are present within M2 and are connected to the previously described horizontal dislocations (Figure 9a). Where the two dislocations are separate, they exhibit different chemical signatures. Branch 1, on the left in Figure 8f, exhibits concentrations of Fe and Al of 1.8 at. % and 0.15 at. %, respectively. Branch 2 yields a slightly stronger enrichment in Fe at 2.1 at. % and higher concentrations of Al at 0.42 at. %. Furthermore, this branch also exhibits concentrations of 0.23 at. % Ca, 0.19 at. % Si and 0.08 at. % Zr.

Where the two dislocations intersect, the Fe and H concentrations increase further relative to the individual branches to 4 at. % and 6 at. %, respectively. The Al concentration also increases slightly compared to the individual branches reaching 0.45 at. %, while Ca, Si and Zr concentrations remain at the same levels as in Branch 2 (Figure 10). To better visualize the difference between the two branches and the intersection points, a 1D concentration profile crossing both branches and moving along the entire length of the dislocations was recorded (Data S3, DR-3). Note that all elements reach their maximum concentration in the centre of the isoconcentration surface (Figure 9f); all elements are co-located and do not form a core-shell structure as seen for high-angle boundaries (Fougerouse et al., 2019).

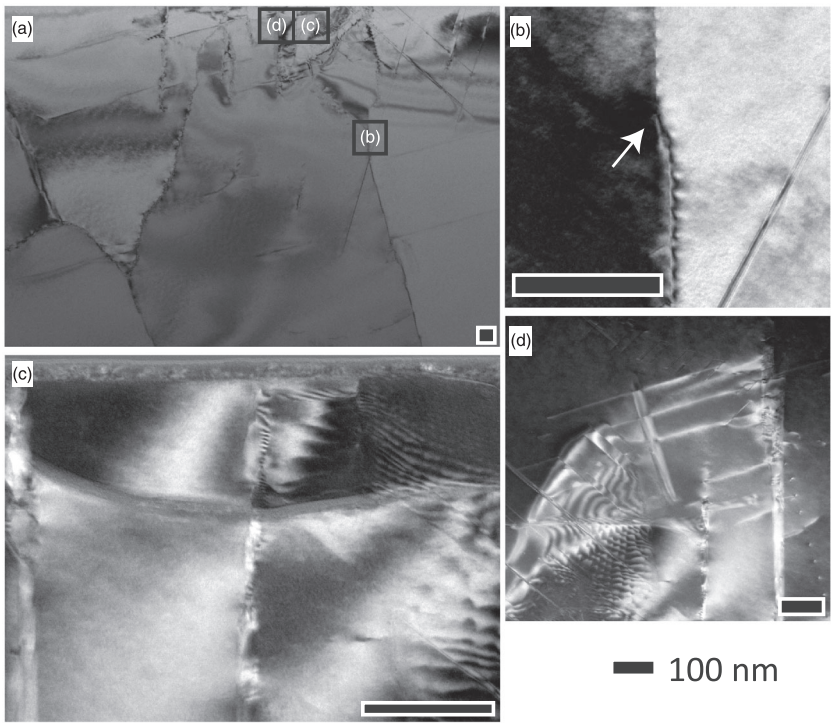

FIGURE 8 TEM images from the same ROI as the APT specimens. (a) TEM HAADF image showing the complexity of the microstructures present within deformed rutile. (b) TEM HAADF and (c, d) TEM dark-field images showing the low-angle boundaries in greater detail. The white arrow in (b) indicates the offset of an otherwise continuous LAB. Note the slight changes in orientation of the LAB similar to the change in the TKD maps in the APT needles.

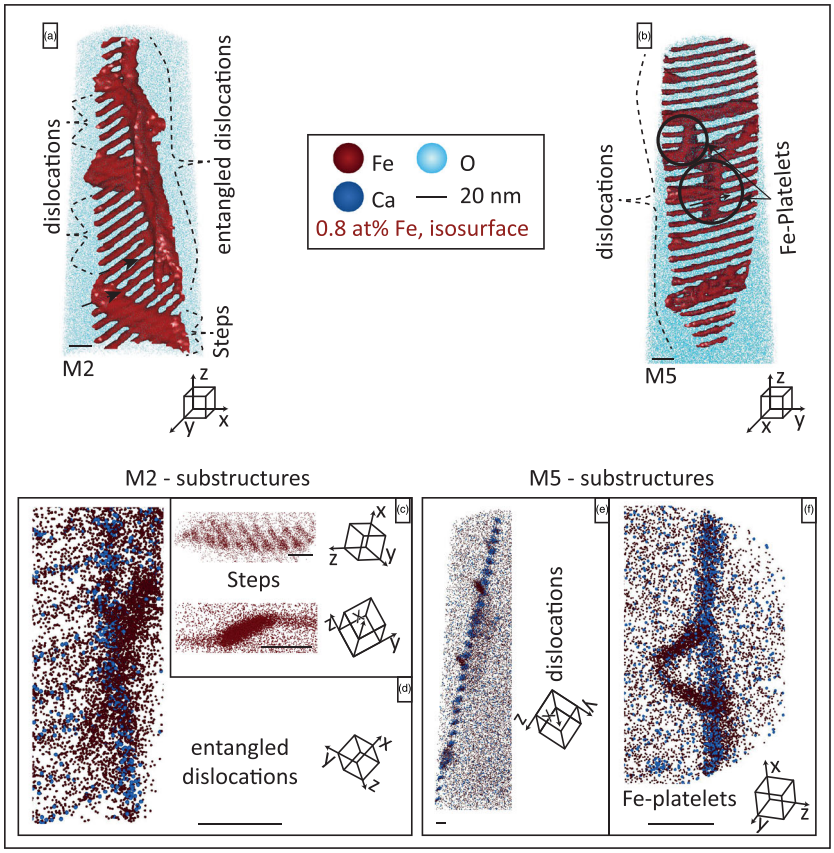

FIGURE 9 Three-dimensional digital reconstruction of APT specimens 1 and 2. (a, b) Isoconcentration surfaces of Fe with several substructures labelled. (c) Top and side view of the 'steps' showing the resulting offset of approximately 10 nm. These 'steps' are also visible in (e) where they are free of any Ca enrichment. (d) Two entangled dislocations, of which one is in direct contact with the dislocations that form the LAB. Note the difference in Ca distribution between the two dislocations (Video S2, DR-5). (e) View of the low-angle boundary along the dislocation cores showing the distribution of Fe and Ca. (f) View along the dip of the low-angle boundary in M5 showing the two Fe-platelets extending from the LAB. The acute angles between the two platelets and the boundary are approximately 60°. The black arrows in a and b refer the measurement location 1D concentration profiles (Figure 10). [Colour figure can be viewed at wileyonlinelibrary.com]

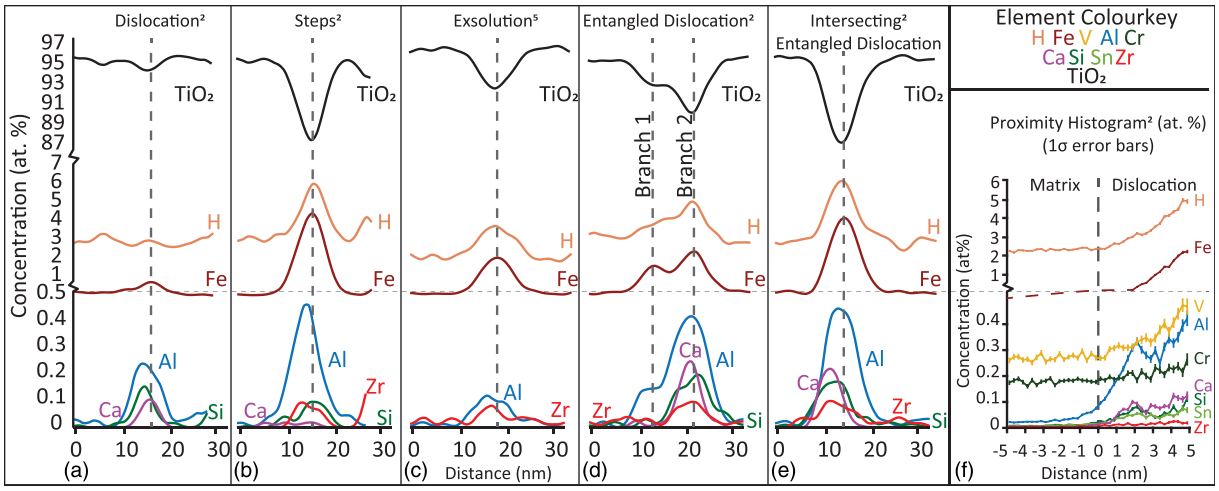

FIGURE 10 Concentration profiles for the several substructures observed in the 3D APT reconstruction. The index number refers to the specimen number (M2 or M5). (a–e) One-dimensional concentration profile through single substructures observed in APT specimens 1 and 2. (f) Proximity histogram for the full low-angle boundary. The location for the measurement is indicated in the reconstructions in Figure 9 and Video S2, DR-5 [Colour figure can be viewed at wileyonlinelibrary.com]

Proximity histograms can visualize the overall extent of trace-element enrichment (Figure 10f). The TiO_2 concentration is approximately 96 at. % in the matrix and decreases by approximately 5 at. % within the substructures. The Fe concentration increases from approximately 0.1 at. % to 2.3 at. %, and the H signal increases from approximately 2.3 at. % to 4.2 at. %, together making up the bulk of trace-element enrichment. Furthermore, V increases from approximately 0.26 at. % to 0.45 at. %, and Cr concentrations increase from approximately 0.17 at. % to 0.26 at. %. Al, Ca, Si and Sn are present in concentrations of <0.025 at. % within the matrix but reach

concentrations of 0.42, 0.12, 0.12 and 0.07 at. %, respectively, within the substructures. Zr, important for temperature estimations, is present in concentrations of <0.01 at. % in the matrix but increases to 0.025 at. % within features in the low-angle boundary.

5 | DISCUSSION

5.1 | Relative timing and conditions of geological events

Before assessing the influence of LABs and associated dislocations on rutile geochemistry, the relative timing of growth and deformation, and the *P*–*T* conditions during both, must be constrained. These constraints also help to assess the potential for volume diffusion, allowing us to distinguish other transport mechanisms. Omphacite within the rutile-bearing vein contains coesite inclusions (Figure 4b), whereas quartz inclusions are preserved inside the investigated rutile grains (Figure 4c). These inclusions indicate that (1) the vein formed at ultrahigh-pressure metamorphic conditions and (2) rutile growth occurred within the quartz stability field, thus not during the UHP metamorphic peak. The Zr concentrations in rutile (Figure 5) correspond to temperatures that are either on the high-pressure prograde path or low-pressure retrograde path. No evidence is observed for significant mineral reactions or overprinting at the intersection of Zr-in-rutile temperatures and the retrograde path for the LCU. Therefore, based on estimated *P*–*T* conditions of rutile growth from Groppo et al. (2009) and constraints from Zr-in-rutile thermometry, a post-UHP timing of rutile growth can be ruled out.

Here, quartz is present as inclusions in rutile, and both zircon and coesite are present as inclusions within the surrounding omphacite grains (Figure 4). Although no zircon inclusions were identified in the rutile, it has been established that zircon is a ubiquitous accessory mineral in the mineral assemblage of the Lago di Cignana eclogites (King et al., 2004). Therefore, we can safely assume that $a_{Si} = a_{Zr} = 1$ during rutile growth, thereby satisfying the requirements for accurate Zr-in-rutile thermometry. The pressure range of rutile growth is estimated to be 2.3–2.8 GPa based on the quartz-coesite transition as an upper limit. The lower limit is based on the timing of rutile growth relative to garnet growth and *P*–*T* conditions obtained for the latter (Groppo et al., 2009). The resulting temperature range of 510–565 (± 20)°C agrees with the prograde *P*–*T* conditions determined by Groppo et al. (2009). Determining the timing of deformation of rutile and omphacite is problematic due to a lack of constraints. However, deformation after the metamorphic peak was limited, as exhumation coincided with the localization of deformation into shear bands (van der Klauw et al., 1997), which are lacking in the omphacite vein studied here.

The formation of Fe-platelets in rutile (Figure 3b) is a common process that takes place in response to exhumation and cooling (Putnis, 1978). This exsolution is an unmixing process that reduces the energy of an oversaturated solution. Here, the presence of these Fe-bearing exsolution products is explained by cooling associated with the rapid exhumation of this Alpine region after the metamorphic peak at 45–41 Ma (Amato et al., 1999; Gouzu et al., 2016; Reddy et al., 1999; Rubatto et al., 1998).

Before assessing the role of microstructures in the mobility of trace elements, volume diffusion must be considered for reference (Figure 11). Because the rate of bulk/volume diffusion is exponentially temperature dependent, the majority of diffusion will have taken place at (near-) peak metamorphic temperature, which is 590–630°C in the case of the LCU (Groppo et al., 2009; Reinecke, 1998). An estimate of the duration of (near-) peak temperatures duration can be made based on various geochronology data (Section 2.1). Relevant ages are compiled into an overview in Figure 11a. Assuming 44 Ma as the onset of peak temperatures (Rubatto et al., 1998) and 36 Ma as cooling below this temperature during exhumation (Reddy et al., 2003), the maximum duration of (near-) peak temperature is 8 Myr and possibly shorter than 5 Myr (Gouzu et al., 2016).

5.2 | Crystal-plastic deformation of rutile

Intragranular distortion in rutile occurred by dislocation creep and resulted in the formation of LABs within the crystal. For rutile, only a few studies report on natural deformation microstructures (Moore et al., 2020; Plavsa et al., 2018). However, the activation of the slip systems in rutile has been studied experimentally since the early 1960s. These studies revealed activation of the {101}<−101> and {110}<001> slip systems depending on crystal orientation (Ashbee & Smallman, 1963; Hirthe & Brittain, 1963). Later studies reported activation of the {101}<−101> and {110}<001> slip systems to be temperature-dependent with activation occurring at 600°C and 900°C, respectively (Blanchin et al., 1990), under experimental stresses and strain rates. The presence of both these slip systems is also in agreement with experimental results on the effect of indentation on the (001) (Basu et al., 2012). Furthermore, results from a more recent study on natural rutile samples by Moore et al. (2020) demonstrated that activation of {110}<001> can occur

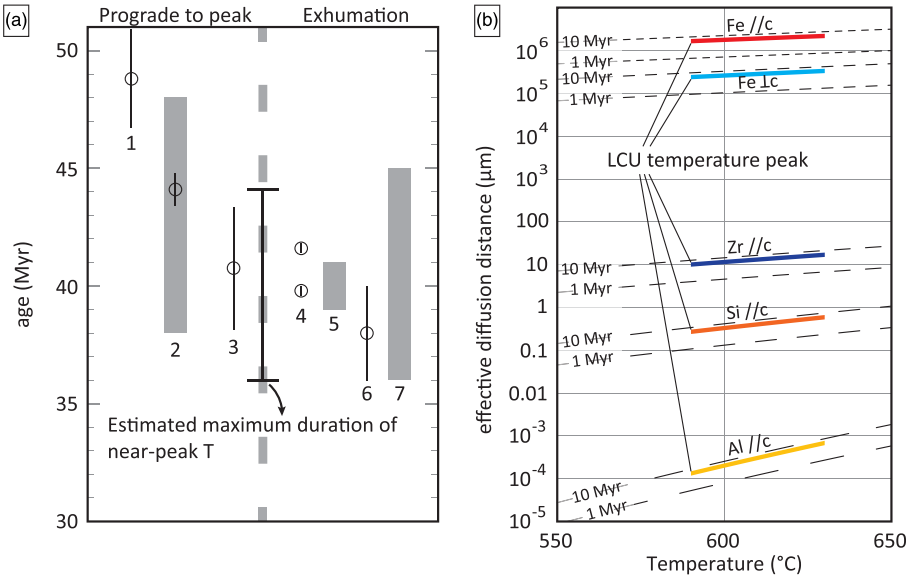

FIGURE 11 (a) Overview of geochronology literature for prograde-to-peak metamorphism of Lago di Cignana and early exhumation for neighbouring units. Error bars are given as reported in literature; grey bars indicate a range of a whole dataset. Data sets and references: (1) Lapen et al. (2003), whole rock-garnet-clinopyroxene Lu-Hf; (2) Rubatto et al. (1998), zircon U/Pb; (3) Amato et al. (1999), whole rock-garnet Sm-Nd; (4) Skora et al. (2015), phengite-clinozoisite Rb-Sr; (5) Gouzu et al. (2016), white mica K-Ar; (6) Amato et al. (1999), whole rock-phengite Rb-Sr; (7) Reddy et al. (1999), phengite and miscellaneous other minerals Rb-Sr. (b) Overview of effective diffusion distance for various relevant elements in rutile, as function of peak T of the LCU and the estimated duration thereof (5–8 Myr). Solid lines indicate effective diffusion distances in rutile of Fe, Zr, Al and Si parallel to the *c* axis and Fe perpendicular to the *c* axis. Dashed lines indicate effective diffusion distances for fixed durations of peak temperature of 1 and 10 Myr. [Colour figure can be viewed at wileyonlinelibrary.com]

below 900°C, presumably due to strain rates that are lower in nature than in experiments.

The microstructural analysis of rutile by EBSD shows the presence of LABs with misorientation axes parallel to <100> and <110>, indicating the presence of tilt walls formed by the climb of edge dislocations on the {100}<001> and {110}<001> slip system. Considering that M2 and M5 were prepared from the same LAB, the multiple misorientation axes show that this boundary is segmented. The UHP-LT (>2.7 GPA, ~600°C) metamorphic conditions suggest that the temperature threshold of ≤600°C for this slip system at typical natural stresses and strain rates (Blanchin et al., 1990) is lower than indicated in early experimental studies. This would be in agreement with the conclusion of Moore et al. (2020) on the {110}<001> slip system.

5.3 | Formation of nanoscale substructures

The LABs observed by EBSD were targeted for APT and TEM analyses, which revealed a complex underlying substructure. Evenly spaced linear features lie consistently within the plane of the LAB. The geometry, size and spacing of these features suggest that they are dislocations and are therefore intrinsic to the LAB (Hirth & Balluffi, 1973). APT studies on LABs have previously observed similar features in zircon (Piazolo et al., 2016; Reddy et al., 2016) and titanite (Kirkland et al., 2018). In rutile, the geometry of linear features in the LAB is comparable with dislocations observed in twin boundaries in rutile (Reddy et al., 2020; Verberne et al., 2022). The spacing between dislocations, as well as the diameter of the zone of enrichment in trace-elements, varies between the materials. The enriched zone consists of the dislocation core and a surrounding area of lattice distorted by elastic strain and associated stresses, indicating that the enriched zone constitutes a Cottrell atmosphere (Cottrell & Bilby, 1949). The capture of trace elements in the Cottrell atmosphere reduces the stress fields. In minerals, studies by APT show that the enrichment zone extends for approximately 3–5 nm in zircon (Piazolo et al., 2016) and 10–24 nm in titanite (Kirkland et al., 2018). In this study, dislocations in rutile have an enriched zone of trace elements of 8–10 nm in diameter, similar to the dislocations observed in twin boundaries (Reddy et al., 2020, Verberne et al., 2022). Relative to

their respective Burgers vector (*b*), these enriched zones have a diameter of approximately 17*b*–33*b* in the rutile, 4*b*–8*b* in zircon and 11*b*–33*b* in titanite, depending on the direction of the Burgers vector. Modelling of Cottrell atmospheres in metallic samples (Ni) with hydrogen as solute/trace element yields diameters of approximately 12*b* (Sills & Cai, 2018). The stress field around dislocations and variances in the material could cause the difference in how far from the core a Cottrell atmosphere can extend and put a limit on the maximum concentration of trace elements around a dislocation (Cochardt et al., 1955). Furthermore, the difference in the electric field around the dislocation and the host material in each mineral when exposed during APT analysis and differences in reconstruction parameters could lead to a magnifying effect on the observed radius of the Cottrell atmosphere (Fougerouse et al., 2016; Vurpillot et al., 2000).

The dislocations that form the LAB lie on a plane that is offset by intervals of approximately 10 nm, referred to as 'steps' (Figures 8b and 9c,d). Such a structure was not observed in previous APT analyses of LABs in zircon (Piazolo et al., 2016; Reddy et al., 2016) and titanite (Kirkland et al., 2018). The dislocations are still visible within these steps (Figure 9c), suggesting that the steps formed during crystal-plastic deformation or when the dislocations were pinned in place. It is unlikely that this feature is a set of dislocations that is intersecting the LAB on a different slip system. This configuration would not result in the offset of the LAB itself, and the dimensions of this feature do not fit with the other dislocations observed in this and previous studies of rutile (Kuzmina et al., 2015; Reddy et al., 2020; Verberne et al., 2022). Instead, this feature is interpreted to reflect a long-period (chemical) stacking order (LPSO) (Inoue et al., 2001). LPSOs are known in the material sciences and are formed as a mechanism for strain accommodation in a chemically enriched region (Abe et al., 2002; Furuhara & Gu, 2013; Inoue et al., 2001). It is therefore expected that nucleation of these structural sites occurs on an existing array of dislocations. The chemical ordering is then achieved by the local strain field around the dislocations enhancing the diffusion of trace elements (Abe et al., 2002).

5.4 | Mechanisms for element mobility

The diffusion of Zr in rutile parallel to the *c* axis, the direction of fastest diffusion, has been studied experimentally at temperatures in the range 750–1,100°C (Cherniak et al., 2007). Extrapolation of the Arrhenius equation in Cherniak et al. (2007) gives the effective diffusion distance for Zr in rutile over temperatures and durations representative of peak metamorphism of the LCU (Figure 11). For comparison, the effective diffusion distance is also given for Fe parallel and perpendicular to the *c* axis based on a temperature-dependent power law of experimentally obtained diffusion coefficients by Sasaki et al. (1985). Fe diffuses several orders of magnitude faster than Zr and, with an effective diffusion distance of 0.2–4.5 m, should be homogenized throughout the rutile crystals. In contrast, the upper limit for the effective diffusion distance of Zr is approximately 20 μm, thus limiting homogenization. Based on the work by Cherniak et al. (2007) and Dohmen et al. (2019), the temperature at which Zr diffusion in rutile becomes negligible for Zr-in-rutile thermometry is around 600–650°C. This temperature range is in agreement with the short effective diffusion distance for Zr estimated for the LCU. Al and Si, two elements that are enriched within the LABs (Figure 10), are experimentally demonstrated to diffuse significantly slower than other elements in rutile at high temperatures (Cherniak & Watson, 2019). This difference in diffusivity also holds up when extrapolating diffusion coefficients to temperatures relevant to the LCU (Figure 11).

The presence of the nanoscale substructures in the low-angle boundary that are chemically and structurally different from each other suggests that different mechanisms for trace-element mobility were potentially active at the same time. Low-angle boundaries form by stress-induced glide and climb (Dhanaraj et al., 2010); therefore, four main mechanisms need to be evaluated: the effectiveness of volume diffusion and transport to the LAB, the potential for fast-diffusion pathways or trace element trapping in dislocation and the dislocation-impurity pair migration. Previous APT studies demonstrated that information on the active diffusion mechanisms could be derived from the APT datasets and correlative analysis. Volume diffusion in combination with U-decay effects results in the formation of Pb enriched clusters (Peterman et al., 2016, 2019; Valley et al., 2014, 2015; Verberne et al., 2020). Fast-diffusion pathways in the form of low- and high-angle and twin boundaries allow for element migration (Fougerouse et al., 2018, 2019; Piazolo et al., 2016); however, these also have been shown to act as trace-element traps (Verberne et al., 2022), and dislocation-impurity pair migration was suggested to lead to trace-element enrichment in titanite (Kirkland et al., 2018) and pyrite (Dubosq et al., 2019).

Here, APT revealed that the features associated with the LAB are enriched in common trace elements (e.g., Fe, Zr, Si and Al) and, in the case of the dislocations composing the LAB and one orthogonal dislocation, also

in uncommon Ca. The presence of Fe and other trace elements with an affinity for rutile in the nanoscale substructure might reflect the capture of trace elements in the strain field around dislocations (Cottrell & Bilby, 1949). The models for volume diffusion (Figure 11) indicate that Fe and Zr both could diffuse into the dislocations during peak metamorphism. The subsequent migration of dislocations into the LAB would result in enrichment of the LAB in trace elements (Dubosq et al., 2019; Imai & Sumino, 1983; Petukhov & Klyuchnik, 2012). Alternatively, these elements could be derived from the grain exterior (Fougerouse et al., 2019; Joesten, 1991; Kirkland et al., 2018), which would result in a question regarding whether the dislocations behaved as an element trap, as a pathway for diffusion, or both.

Besides trace elements that are common in rutile, the dislocations are decorated in Ca. Ca has no affinity for rutile and is not expected to be incorporated within the crystal lattice during growth. Reports on Ca in rutile attributed its apparent presence to potential interference with the surrounding Ca-bearing silicate phases (Zack et al., 2002). Rutile standards for LA-ICP-MS, such as R10 (Luvizotto et al., 2009), also lack values for Ca calibration. LA-ICP-MS data in this study (Data S3, DR3) generally did not indicate Ca in rutile above detection limits of between 14 and 139 ppm. The lack of Ca in the rutile matrix rules out volume diffusion and dislocation-impurity pair diffusion as mechanisms for Ca enrichment in dislocations. Besides Ca enrichment around dislocations, volume diffusion would have resulted in enrichment of the rutile matrix, and without Ca in the matrix, no ions can be captured in the strain field of the dislocations. The ionic sizes of elemental species in part control element migration, and therefore, it can be questioned whether large cations such as Ca can migrate into the region of elastic strain around a dislocation from the matrix (Cottrell & Bilby, 1949; Kirkland et al., 2018; Shannon, 1976).

The rutile grain resides within an omphacite vein also including apatite and glaucophane, indicating that Ca was readily available during vein formation. The fluid from which the omphacite vein formed is a probable source for the Ca, which was likely incorporated in the rutile by diffusion along the LABs.

Si and Al are enriched in the LABs alongside Ca but are more readily incorporated in rutile and thus do not require an external source (Figure 5). However, Si and Al are known to migrate by volume diffusion at significantly lower rates in rutile than other elements (Figure 11b; Cherniak & Watson, 2019). The affinity of these elements for LABs without the possibility for their enrichment through volume diffusion at the temperature and timescale of the LCU indicates a different mechanism of incorporation. This mechanism could be similar to Ca, namely, incorporation and transport from an external source into the grain interior along LABs, or otherwise by dislocation-impurity migration.

Trace-element enrichment by fast diffusion along dislocations, or 'pipe' diffusion (Love, 1964), has been suggested in previous APT studies on minerals to facilitate the removal of Pb in zircon (Piazolo et al., 2016) or allow for the incorporation of K, a large cation, in titanite (Kirkland et al., 2018). Therefore, we interpret the Ca decorating the dislocations in rutile as externally derived and to have been incorporated into the low-angle boundary by enhanced diffusivity along dislocations.

The lack of Ca in one of the vertically orientated dislocations and the steps (Figures 9 and 10) further suggests that Ca incorporation predated these dislocations or was energetically unfavourable. Migrating dislocations can be entangled, resulting in core–core and overlap leading to enrichment in trace elements, as demonstrated for pyrite (Fougerouse et al., 2019). Here, the simplest explanation would be that a migrating dislocation becomes entangled and pinned on the pre-existing Ca-rich dislocations. The lack of Ca in the Ca-free dislocation suggests that diffusion of large cations like Ca became ineffective before this entanglement.

The impact of intragranular substructure on rates of diffusion needs to be considered as dislocations can act as fast diffusion pathways or traps for trace elements. An effective diffusion distance of 10 μm (Figure 11) allows for the mobilization of Zr into the LAB network for much of the grain interior (Figure 6). The question becomes whether Zr is retained or mobilized along the dislocations. Recent APT studies on rutile show that while Zr might be able to migrate along dislocations, the diffusivity of Zr along dislocations is still slow (Verberne et al., 2022). It was, therefore, suggested that dislocations mainly act as a trap for mobile Zr, thus preserving bulk Zr concentrations, albeit in a more localized form.

Trace-element enrichment is highest in the dislocation cores, with lower concentrations of impurities further away from the dislocation cores. This distribution is consistent with observations of H in Ni (Sills & Cai, 2018). In the 'steps' and where the entangled dislocations intersect, the difference in concentration between the rutile matrix and features is approximately 6 at. %. While not matching a known different mineral phase, a 6 at. % difference in composition raises the question of whether these features should be considered rutile or a discrete, thermodynamically stable phase. Similar features, though in higher concentrations, have been described as linear complexions (Kuzmina et al., 2015).

5.5 | Implications for Zr-in-rutile geothermometry

The influence of Zr present within a LAB on composition measurements by various techniques can be predicted (Figure 12), although it remains an open question as to whether Zr is retained or migrates along dislocations. Figure 12 shows the modelled results for Zr-in-rutile thermometry that would be obtained by techniques with different spatial resolution and plots the atomic concentration of Zr against temperature. Zr-in-rutile thermometry is calibrated for the Zr concentration in weight percentages. Thus, the substitution of Ti and O for any other element will barely affect the measured Zr concentration. Here, it is shown that dislocations and other substructures linked to the LAB can result in the exchange of 1–8 at. % Ti for other trace elements (Figure 10). However, this compositional modification is very localized. Hence, the spatial resolution of the analytical technique used for measuring Zr concentration may play a critical role in determining the measured concentrations. In Figure 12, we assess the influence of the spatial resolutions of different techniques on Zr-in-rutile thermometry under the following assumptions:

1. The chemical system is simplified assuming a composition of $Ti_{1-x}O_2$, where x is only Zr.
2. The Zr concentration in the LAB is based on the proximity diagram of this study (0.01 at. %)
3. 'Measurements' are acquired on surfaces perpendicular to the LAB and are centred on the LAB.
4. The length and depth of the LAB are equal to the spot size (d) diameters and analytical depth. The width of the LAB is equal to the diameter of the zone of chemical enrichment around dislocations (y) visualized by APT.
5. The volume of the LAB within the spot analysis is simplified to be *length* (l)**width* (w)**depth* (h), ignoring the curvature at the edges.
6. The apparent composition of the LAB is a mix between the composition of the dislocations and that of the remaining volume in the LAB assumed to have the composition of the matrix. The contributions of dislocations and matrix to the composition of the LAB are set to 50% each based on the isoconcentration profiles of Specimens 1 and 2 (Figure 9).

From the above assumptions, the proportion of matrix sampled by a given spot size is

$$\left(1-\frac{4y}{\pi d}\right). \quad (1)$$

Assuming that the matrix Zr concentration represents the 'true value' (Figure 12), the red line indicates the

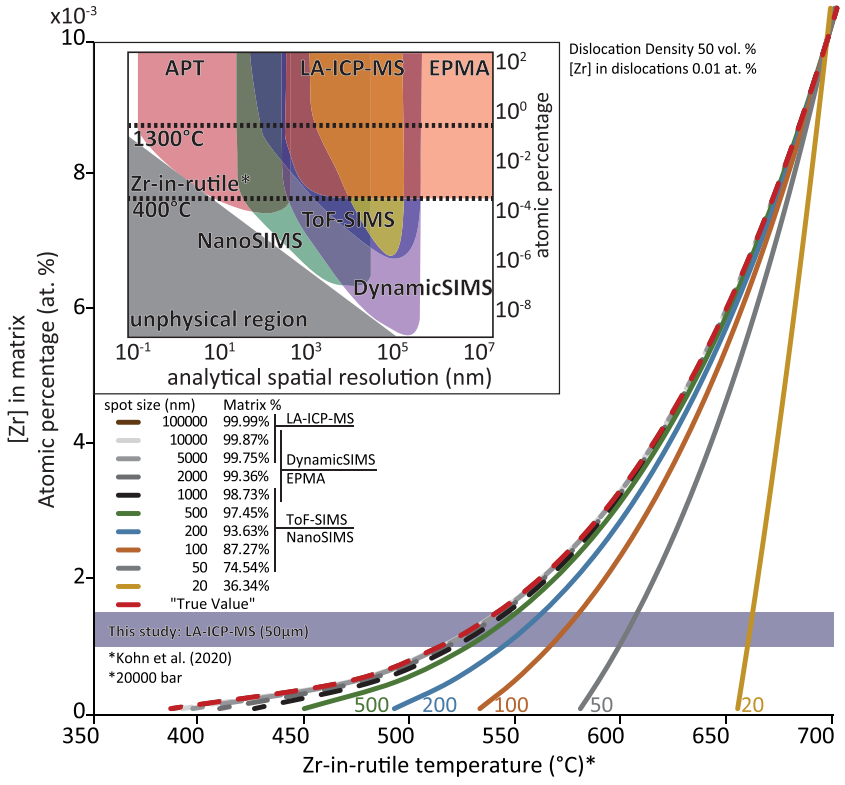

FIGURE 12 Temperatures obtained by Zr-in-rutile thermometry, and how these are affected by Zr-enriched LABs, as a function of Zr in the rutile matrix. Several spot sizes of the hypothetical chemical analysis are displayed along with the percentage of the sampled volume that consists of matrix. The inset is a diagram of the range of analytical resolution and detection limit for chemical analysis techniques used in geosciences. Element concentrations corresponding to two extreme temperatures for the application of Zr-in-rutile are given as context. APT, atom probe tomography; EPMA, electron probe micro analysis; LA-ICP-MS, laser ablation inductively coupled plasma mass spectrometry; SIMS, secondary ion mass spectrometry; ToF, time of flight [Colour figure can be viewed at wileyonlinelibrary.com]

expected temperature for a given concentration. The other profiles represent the measurements based on analysis with different spot sizes, measuring a volume that contains a Zr-enriched LAB. The smaller analytical volumes measure relatively less matrix. With increasing temperature, these temperature profiles converge to the point where the concentration of Zr in dislocations matches the concentration of Zr in the matrix. At even higher concentrations of Zr in the matrix, the profiles these would diverge as a lower Zr concentration in the LAB compared to the matrix would lead to a lower estimate of the temperature.

Here, we observed an enrichment of Zr in the LABs. Zr-in-rutile temperatures calculated from analyses performed with a spot size >1 μm are not influenced by the Zr enrichment of the LAB due to the volume of matrix material measured being far greater than the volume of dislocations. For the measurements performed in this study, LA-ICP-MS with a 50 μm spot size, the temperatures are representative. Analytical techniques with spot sizes less than 1 μm overestimate the temperature, becoming more significant around a spot size of 200 nm. If it is assumed Zr was removed from the rutile via the LAB network, spot sizes <1 μm might provide more accurate Zr-in-rutile temperatures if the beam intersects a subgrain boundary. However, current models are not calibrated for the properties of dislocations.

Based on the work done in this study, the demonstration of trapping of Zr and the literature (Clark et al., 2019), it is again clear that Zr-in-rutile geothermometry is a robust technique, including at low temperatures and (U)HP conditions. Analytical techniques with a relatively low spatial resolution such as LA-ICP-MS are ideal for the measurement of Zr concentration. However, when it can be demonstrated that diffusion caused the loss of Zr via bulk diffusion, high spatial resolution techniques incorporating microstructures could provide more accurate results or a better range of temperature estimates because of the trapping of Zr in dislocations.

6 | SUMMARY

The rutile analysed in this study records prograde growth and was thereafter incorporated in a peak-metamorphic omphacite vein that formed at ultra-high pressure conditions. The rutile was deformed in between these two events, resulting in the formation of low-angle boundaries by dislocations predominantly on the {100}[001] slip systems. The dislocations that constitute the low-angle boundary are enriched in trace elements and form several structures as revealed in the 3D APT data. Fe, Ca, Zr, Al and Si are found at elevated concentrations in these boundaries. The enrichment of those elements except Fe cannot be explained by solely assuming volume diffusion. Pipe diffusion via these deformation structures likely played a role in the redistribution of trace elements, potentially from the grain exterior in the case of Ca. The enrichment of low-angle boundaries needs to be considered when applying geochemistry to deformed minerals, as it can lead to faster re-equilibration by diffusion, and it can affect measurements targeting the crystal matrix. Measuring trace element concentrations (e.g., Zr) by techniques with high-spatial resolution can lead to significant overestimations of the concentration compared to bulk (>50°C for Zr-in-rutile).

ACKNOWLEDGEMENTS

Work was conducted within the Geoscience Atom Probe Facility at Curtin University and part of the Advanced Resource Characterisation Facility (ARCF). The ARCF, under the auspices of the National Resource Sciences Precinct (NRSP)—a collaboration between CSIRO, Curtin University and The University of Western Australia—is supported by the Science and Industry Endowment Fund (SIEF). The authors gratefully acknowledge support of Curtin University's Microscopy and Microanalysis Facility and the John de Laeter Centre, whose instrumentation has been supported by University, State and Commonwealth Government funding. H.W. v.S.L. and M. A. acknowledge funding received from the European Research Council under the European Union's Horizon 2020 research and innovation program grant agreement 714936 to M. Alvaro. S.M. Reddy and D.W. Saxey acknowledge funding through the Australian Research Council (DP210102625). Marco Scambelluri is acknowledged for valuable feedback on this work. We are grateful to Elias Bloch and Sandra Piazolo for thoughtful and in-depth reviews that greatly improved the manuscript.

ORCID

Rick Verberne https://orcid.org/0000-0002-5529-1250
Hugo W. van Schrojenstein Lantman https://orcid.org/0000-0002-9100-9961
Steven M. Reddy https://orcid.org/0000-0002-4726-5714
David Wallis https://orcid.org/0000-0001-9212-3734
Antonio Langone https://orcid.org/0000-0002-7346-2922

REFERENCES

Abe, E., Kawamura, Y., Hayashi, K., & Inoue, A. (2002). Long-period ordered structure in a high-strength nanocrystalline Mg-1 at% Zn-2 at% Y alloy studied by atomic-resolution Z-contrast STEM. *Acta Materialia*, *50*(15), 3845–3857. https://doi.org/10.1016/S1359-6454(02)00191-X

Amato, J. M., Johnson, C. M., Baumgartner, L. P., & Beard, B. L. (1999). Rapid exhumation of the Zermatt-Saas ophiolite deduced from high-precision Sm–Nd and Rb–Sr geochronology. *Earth and Planetary Science Letters*, *171*, 425–438. https://doi.org/10.1016/S0012-821X(99)00161-2

Ashbee, K., & Smallman, R. E. (1963). The plastic deformation of titanium dioxide single crystals. *Proceedings of the Royal Society of London. Series A. Mathematical and Physical Sciences*, *274*(1357), 195–205.

Bachmann, F., Hielscher, R., & Schaeben, H. (2010). Texture analysis with MTEX–free and open source software toolbox. Paper presented at the Solid State Phenomena, *160*, 63–68. https://doi.org/10.4028/www.scientific.net/SSP.160.63

Basu, S., Elshrief, O. A., Coward, R., Anasori, B., & Barsoum, M. W. (2012). Microscale deformation of (001) and (100) rutile single crystals under spherical nanoindentation. *Journal of Materials Research*, *27*(1), 53–63. https://doi.org/10.1557/jmr.2011.337

Blanchin, M., Bursill, L., & Lafage, C. (1990). Deformation and microstructure of rutile. *Proceedings of the Royal Society of London A. Mathematical and Physical Sciences*, *429*(1876), 175–202.

Blum, T. B., Darling, J. R., Kelly, T. F., Larson, D. J., Moser, D. E., Perez-Huerta, A., Prosa, T. J., Reddy, S. M., Reinhard, D. A., Saxey, D. W., Ulfig, R. M., & Valley, J. W. (2018). Best practices for reporting atom probe analysis of geological materials. *Microstructural Geochronology: Planetary Records Down to Atom Scale*, *232*, 369–373. https://doi.org/10.1002/9781119227250.ch18

Cherniak, D. (2000). Pb diffusion in rutile. *Contributions to Mineralogy and Petrology*, *139*(2), 198–207. https://doi.org/10.1007/PL00007671

Cherniak, D. J., Manchester, J., & Watson, E. B. (2007). Zr and Hf diffusion in rutile. *Earth and Planetary Science Letters*, *261*(1–2), 267–279. https://doi.org/10.1016/j.epsl.2007.06.027

Cherniak, D. J., & Watson, E. B. (2019). Al and Si diffusion in rutile. *American Mineralogist: Journal of Earth and Planetary Materials*, *104*(11), 1638–1649. https://doi.org/10.2138/am-2019-7030

Clark, C., Taylor, R. J., Johnson, T. E., Harley, S. L., Fitzsimons, I. C., & Oliver, L. (2019). Testing the fidelity of thermometers at ultrahigh temperatures. *Journal of Metamorphic Geology*, *37*(7), 917–934.

Cochardt, A., Schoek, G., & Wiedersich, H. (1955). Interaction between dislocations and interstitial atoms in body-centered cubic metals. *Acta Metallurgica*, *3*(6), 533–537. https://doi.org/10.1016/0001-6160(55)90111-5

Cottrell, A. H., & Bilby, B. (1949). Dislocation theory of yielding and strain ageing of iron. *Proceedings of the Physical Society. Section A*, *62*(1), 49–62. https://doi.org/10.1088/0370-1298/62/1/308

Crameri, F. (2018). Scientific colour-maps. *Zenodo*, 10. https://doi.org/10.5281/zenodo.1243862

Cutts, J., & Smit, M. (2018). Rates of deep continental burial from Lu-Hf garnet chronology and Zr-in-rutile thermometry on (ultra) high-pressure rocks. *Tectonics*, *37*(1), 71–88. https://doi.org/10.1002/2017TC004723

Dachille, F., Simons, P., & Roy, R. (1968). Pressure-temperature studies of anatase, brookite, rutile and TiO2-II. *American Mineralogist*, *53*, 1929–1939.

DesOrmeau, J. W., Gordon, S. M., Little, T. A., Bowring, S. A., & Chatterjee, N. (2017). Rapid time scale of Earth's youngest known ultrahigh-pressure metamorphic event, Papua New Guinea. *Geology*, *45*(9), 795–798. https://doi.org/10.1130/G39296.1

Dhanaraj, G., Byrappa, K., Prasad, V. V., & Dudley, M. (2010). Crystal growth techniques and characterization: An overview. In G. Dhanaraj, K. Byrappa, V. Prasad, & M. Dudley (Eds.), *Springer Handbook of Crystal Growth*. Springer Handbooks. Springer. https://doi.org/10.1007/978-3-540-74761-1_1

Dohmen, R., Marschall, H. R., Ludwig, T., & Polednia, J. (2019). Diffusion of Zr, Hf, Nb and Ta in rutile: Effects of temperature, oxygen fugacity, and doping level, and relation to rutile point defect chemistry. *Physics and Chemistry of Minerals*, *46*(3), 311–332. https://doi.org/10.1007/s00269-018-1005-7

Dubosq, R., Rogowitz, A., Schweinar, K., Gault, B., & Schneider, D. A. (2019). A 2D and 3D nanostructural study of naturally deformed pyrite: Assessing the links between trace element mobility and defect structures. *Contributions to Mineralogy and Petrology*, *174*(9), 72. https://doi.org/10.1007/s00410-019-1611-5

Forster, M., Lister, G., Compagnoni, R., Giles, D., Hills, Q., Betts, P., Beltrando, M., & Tamagno, E. (2004). Mapping of oceanic crust with "HP" to "UHP" metamorphism: The Lago di Cignana Unit, (Western Alps). In *Mapping geology in Italy*. Geological Society of London.

Fougerouse, D., Reddy, S. M., Aylmore, M., Yang, L., Guagliardo, P., Saxey, D. W., Rickard, W. D., & Timms, N. (2021). A new kind of invisible gold in pyrite hosted in deformation-related dislocations. *Geology*, *49*(10), 1225–1229. https://doi.org/10.1130/G49028.1

Fougerouse, D., Reddy, S. M., Kirkland, C. L., Saxey, D. W., Rickard, W. D., & Hough, R. M. (2019). Time-resolved, defect-hosted, trace element mobility in deformed Witwatersrand pyrite. *Geoscience Frontiers*, *10*(1), 55–63. https://doi.org/10.1016/j.gsf.2018.03.010

Fougerouse, D., Reddy, S. M., Saxey, D. W., Erickson, T. M., Kirkland, C. L., Rickard, W. D. A., Seydoux-Guillaume, A.-M., Clark, C., & Buick, I. S. (2018). Nanoscale distribution of Pb in monazite revealed by atom probe microscopy. *Chemical Geology*, *479*, 251–258. https://doi.org/10.1016/j.chemgeo.2018.01.020

Fougerouse, D., Reddy, S. M., Saxey, D. W., Rickard, W. D., van Riessen, A., & Micklethwaite, S. (2016). Nanoscale gold clusters in arsenopyrite controlled by growth rate not concentration: Evidence from atom probe microscopy. *American Mineralogist*, *101*(8), 1916–1919. https://doi.org/10.2138/am-2016-5781CCBYNCND

Fougerouse, D., Saxey, D. W., Rickard, W. D., Reddy, S. M., & Verberne, R. (2021). Standardizing spatial reconstruction parameters for the atom probe analysis of common minerals. *Microscopy and Microanalysis*, *28*(4), 1221–1230.

Frezzotti, M., Selverstone, J., Sharp, Z., & Compagnoni, R. (2011). Carbonate dissolution during subduction revealed by diamond-bearing rocks from the Alps. *Nature Geoscience*, *4*(10), 703–706. https://doi.org/10.1038/ngeo1246

Furuhara, T., & Gu, X. (2013). Discussion on strain accommodation associated with formation of LPSO structure. *Materials*

Transactions, *54*(5), 675–679. https://doi.org/10.2320/matertrans.MI201224

Gao, X. Y., Zheng, Y. F., Xia, X. P., & Chen, Y. X. (2014). U-Pb ages and trace elements of metamorphic rutile from ultrahigh-pressure quartzite in the Sulu orogen. *Geochimica et Cosmochimica Acta*, *143*, 87–114. https://doi.org/10.1016/j.gca.2014.04.032

Gault, B., Moody, M. P., Cairney, J. M., & Ringer, S. P. (2012). *Atom probe microscopy* (Vol. 160). Springer Science & Business Media. https://doi.org/10.1007/978-1-4614-3436-8

Gouzu, C., Yagi, K., Thanh, N. X., Itaya, T., & Compagnoni, R. (2016). White mica K–Ar geochronology of HP–UHP units in the Lago di Cignana area, western Alps, Italy: tectonic implications for exhumation. *Lithos*, *248*, 109–118. https://doi.org/10.1016/j.lithos.2016.01.015

Groppo, C., Beltrando, M., & Compagnoni, R. (2009). The P–T path of the ultra-high pressure Lago Di Cignana and adjoining high-pressure meta-ophiolitic units: insights into the evolution of the subducting Tethyan slab. *Journal of Metamorphic Geology*, *27*(3), 207–231. https://doi.org/10.1111/j.1525-1314.2009.00814.x

Halama, R., Konrad-Schmolke, M., & de Hoog, J. C. (2020). Boron isotope record of peak metamorphic ultrahigh-pressure and retrograde fluid–rock interaction in white mica (Lago di Cignana, Western Alps). *Contributions to Mineralogy and Petrology*, *175*(3), 1–20. https://doi.org/10.1007/s00410-020-1661-8

Hart, E., Storey, C., Bruand, E., Schertl, H. P., & Alexander, B. D. (2016). Mineral inclusions in rutile: A novel recorder of HP-UHP metamorphism. *Earth and Planetary Science Letters*, *446*, 137–148. https://doi.org/10.1016/j.epsl.2016.04.035

Hart, E., Storey, C., Harley, S. L., & Fowler, M. (2018). A window into the lower crust: Trace element systematics and the occurrence of inclusions/intergrowths in granulite-facies rutile. *Gondwana Research*, *59*, 76–86. https://doi.org/10.1016/j.gr.2018.02.021

Hellman, O. C., Vandenbroucke, J. A., Rusing, J., Isheim, D., & Seidman, D. N. (2000). Analysis of three-dimensional atom probe data by the proximity histogram. *Microscopy and Microanalysis*, *6*(5), 437–444.

Hirth, J. P., & Balluffi, R. W. (1973). On grain boundary dislocations and ledges. *Acta Metallurgica*, *21*(7), 929–942. https://doi.org/10.1016/0001-6160(73)90150-8

Hirthe, W. M., & Brittain, J. O. (1963). High-temperature steady-state creep in rutile. *Journal of the American Ceramic Society*, *46*(9), 411–417. https://doi.org/10.1111/j.1151-2916.1963.tb11767.x

Imai, M., & Sumino, K. (1983). In situ X-ray topographic study of the dislocation mobility in high-purity and impurity-doped silicon crystals. *Philosophical Magazine A*, *47*(4), 599–621. https://doi.org/10.1080/01418618308245248

Inoue, A., Kawamura, Y., Matsushita, M., Hayashi, K., & Koike, J. (2001). Novel hexagonal structure and ultrahigh strength of magnesium solid solution in the Mg–Zn–Y system. *Journal of Materials Research*, *16*(7), 1894–1900. https://doi.org/10.1557/JMR.2001.0260

Jamieson, J. C., & Olinger, B. (1969). Pressure-temperature studies of anatase, brookite rutile, and Ti02 (II): A discussion. *American Mineralogist: Journal of Earth and Planetary Materials*, *54*(9–10), 1477–1481.

Joesten, R. (1991). Grain-boundary diffusion kinetics in silicate and oxide minerals. In *Diffusion, atomic ordering, and mass transport* (pp. 345–395). Springer. https://doi.org/10.1007/978-1-4613-9019-0_11

Keller, L. M., Abart, R., Wirth, R., Schmid, D. W., & Kunze, K. (2006). Enhanced mass transfer through short-circuit diffusion: Growth of garnet reaction rims at eclogite facies conditions. *American Mineralogist*, *91*(7), 1024–1038. https://doi.org/10.2138/am.2006.2068

King, R. L., Bebout, G. E., Kobayashi, K., Nakamura, E., & van der Klauw, S. N. (2004). Ultrahigh-pressure metabasaltic garnets as probes into deep subduction zone chemical cycling. *Geochemistry, Geophysics, Geosystems*, *5*(12). https://doi.org/10.1029/2004GC000746

Kirkland, C., Fougerouse, D., Reddy, S., Hollis, J., & Saxey, D. (2018). Assessing the mechanisms of common Pb incorporation into titanite. *Chemical Geology*, *483*, 558–566. https://doi.org/10.1016/j.chemgeo.2018.03.026

Kirst, F., & Leiss, B. (2017). Kinematics of syn-and post-exhumational shear zones at Lago di Cignana (Western Alps, Italy): Constraints on the exhumation of Zermatt–Saas (ultra) high-pressure rocks and deformation along the Combin Fault and Dent Blanche Basal Thrust. *International Journal of Earth Sciences*, *106*(1), 215–236. https://doi.org/10.1007/s00531-016-1316-1

Klinger, L., & Rabkin, E. (1999). Beyond the Fisher model of grain boundary diffusion: Effect of structural inhomogeneity in the bulk. *Acta Materialia*, *47*(3), 725–734. https://doi.org/10.1016/S1359-6454(98)00420-0

Kohn, M. J. (2020). A refined zirconium-in-rutile thermometer. *American Mineralogist: Journal of Earth and Planetary Materials*, *105*(6), 963–971. https://doi.org/10.2138/am-2020-7091

Kooijman, E., Mezger, K., & Berndt, J. (2010). Constraints on the U-Pb systematics of metamorphic rutile from in situ LA-ICP-MS analysis. *Earth and Planetary Science Letters*, *293*(3–4), 321–330. https://doi.org/10.1016/j.epsl.2010.02.047

Kuzmina, M., Herbig, M., Ponge, D., Sandlöbes, S., & Raabe, D. (2015). Linear complexions: Confined chemical and structural states at dislocations. *Science*, *349*(6252), 1080–1083. https://doi.org/10.1126/science.aab2633

Lapen, T. J., Johnson, C. M., Baumgartner, L. P., Mahlen, N. J., Beard, B. L., & Amato, J. M. (2003). Burial rates during prograde metamorphism of an ultra-high-pressure terrane: An example from Lago di Cignana, western Alps, Italy. *Earth and Planetary Science Letters*, *215*, 57–72. https://doi.org/10.1016/S0012-821X(03)00455-2

Larson, D. J., Prosa, T. J., Ulfig, R. M., Geiser, B. P., & Kelly, T. F. (2013). *Local electrode atom probe tomography*. Springer, New York. https://doi.org/10.1007/978-1-4614-8721-0

Love, G. (1964). Dislocation pipe diffusion. *Acta Metallurgica*, *12*(6), 731–737. https://doi.org/10.1016/0001-6160(64)90220-2

Lund, M. D., Piazolo, S., & Harley, S. L. (2006). Ultrahigh temperature deformation microstructures in felsic granulites of the Napier Complex, Antarctica. *Tectonophysics*, *427*(1–4), 133–151. https://doi.org/10.1016/j.tecto.2006.05.022

Luvizotto, G. L., Zack, T., Meyer, H. P., Ludwig, T., Triebold, S., Kronz, A., Münker, C., Stockli, D. F., Prowatke, S., Klemme, S., Jacob, D. E., & von Eynatten, H. (2009). Rutile crystals as potential trace element and isotope mineral

standards for microanalysis. *Chemical Geology*, *261*(3–4), 346–369. https://doi.org/10.1016/j.chemgeo.2008.04.012

Mei, Z. G., Wang, Y., Shang, S. L., & Liu, Z. K. (2014). First-principles study of the mechanical properties and phase stability of TiO2. *Computational Materials Science*, *83*, 114–119. https://doi.org/10.1016/j.commatsci.2013.11.020

Mezger, K., Hanson, G., & Bohlen, S. (1989). High-precision UPb ages of metamorphic rutile: Application to the cooling history of high-grade terranes. *Earth and Planetary Science Letters*, *96*(1–2), 106–118. https://doi.org/10.1016/0012-821X(89)90126-X

Montalvo, S. D., Reddy, S. M., Saxey, D. W., Rickard, W. D. A., Fougerouse, D., Quadir, Z., & Johnson, T. E. (2019). Nanoscale constraints on the shock-induced transformation of zircon to reidite. *Chemical Geology*, *507*, 85–95. https://doi.org/10.1016/j.chemgeo.2018.12.039

Moore, J., Beinlich, A., Porter, J. K., Talavera, C., Berndt, J., Piazolo, S., Austrheim, H., & Putnis, A. (2020). Microstructurally controlled trace element (Zr, U–Pb) concentrations in metamorphic rutile: An example from the amphibolites of the Bergen Arcs. *Journal of Metamorphic Geology*, *38*(1), 103–127. https://doi.org/10.1111/jmg.12514

Müller, W. F., & Compagnoni, R. (2009). Eclogite from the ultrahigh-pressure metamorphic unit at Lago di Cignana, Western Alps: A process-oriented transmission electron microscope study. *Lithos*, *109*(3–4), 323–332. https://doi.org/10.1016/j.lithos.2008.07.013

Ni, P., Zhu, X., Wang, R., Shen, K., Zhang, Z., Qiu, J., & Huang, J. (2008). Constraining ultrahigh-pressure (UHP) metamorphism and titanium ore formation from an infrared microthermometric study of fluid inclusions in rutile from Donghai UHP eclogites, eastern China. *Geological Society of America Bulletin*, *120*(9–10), 1296–1304. https://doi.org/10.1130/B26090.1

Norman, M., Pearson, N., Sharma, A., & Griffin, W. (1996). Quantitative analysis of trace elements in geological materials by laser ablation ICPMS: Instrumental operating conditions and calibration values of NIST glasses. *Geostandards Newsletter*, *20*(2), 247–261. https://doi.org/10.1111/j.1751-908X.1996.tb00186.x

Oberti, R., & Caporuscio, F. A. (1991). Crystal chemistry of clinopyroxenes from mantle eclogites: A study of the key role of the M2 site population by means of crystal-structure refinement. *American Mineralogist*, *76*(7–8), 1141–1152.

Pearce, N. J., Perkins, W. T., Westgate, J. A., Gorton, M. P., Jackson, S. E., Neal, C. R., & Chenery, S. P. (1997). A compilation of new and published major and trace element data for NIST SRM 610 and NIST SRM 612 glass reference materials. *Geostandards Newsletter*, *21*(1), 115–144. https://doi.org/10.1111/j.1751-908X.1997.tb00538.x

Peterman, E., Reddy, S. M., Saxey, D., Fougerouse, D., Snoeyenbos, D., & Rickard, W. (2019). Nanoscale processes of trace element mobility in metamorphosed zircon. *Contributions to Mineralogy and Petrology*, *174*(11), 92. https://doi.org/10.1007/s00410-019-1631-1

Peterman, E. M., Reddy, S. M., Saxey, D. W., Snoeyenbos, D. R., Rickard, W. D., Fougerouse, D., & Kylander-Clark, A. R. (2016). Nanogeochronology of discordant zircon measured by atom probe microscopy of Pb-enriched dislocation loops. *Science Advances*, *2*(9), e1601318. https://doi.org/10.1126/sciadv.1601318

Petukhov, B., & Klyuchnik, P. (2012). Dynamic interaction of dislocations with impurity subsystem in crystalline materials. *Crystallography Reports*, *57*(3), 388–392. https://doi.org/10.1134/S1063774512030169

Piazolo, S., la Fontaine, A., Trimby, P., Harley, S., Yang, L., Armstrong, R., & Cairney, J. M. (2016). Deformation-induced trace element redistribution in zircon revealed using atom probe tomography. *Nature Communications*, *7*(1), 1–7. https://doi.org/10.1038/ncomms10490

Plavsa, D., Reddy, S. M., Clark, C., & Agangi, A. (2018). Capricorn Orogen rutile study, a combined electron backscatter diffraction (EBSD) and laser ablation split stream (LASS) analytical approach, Record 2018/12, 54p.

Plümper, O., King, H. E., Vollmer, C., Ramasse, Q., Jung, H., & Austrheim, H. (2012). The legacy of crystal-plastic deformation in olivine: High-diffusivity pathways during serpentinization. *Contributions to Mineralogy and Petrology*, *163*(4), 701–724. https://doi.org/10.1007/s00410-011-0695-3

Putnis, A. (1978). The mechanism of exsolution of hematite from iron-bearing rutile. *Physics and Chemistry of Minerals*, *3*(2), 183–197. https://doi.org/10.1007/BF00308121

Reddy, S. M., Saxey, D. W., Rickard, W. D., Fougerouse, D., Montalvo, S. D., Verberne, R., & van Riessen, A. (2020). Atom probe tomography: Development and application to the geosciences. *Geostandards and Geoanalytical Research*, *44*(1), 5–50. https://doi.org/10.1111/ggr.12313

Reddy, S. M., Timms, N. E., Pantleon, W., & Trimby, P. (2007). Quantitative characterization of plastic deformation of zircon and geological implications. *Contributions to Mineralogy and Petrology*, *153*(6), 625–645. https://doi.org/10.1007/s00410-006-0174-4

Reddy, S. M., Timms, N. E., Trimby, P., Kinny, P. D., Buchan, C., & Blake, K. (2006). Crystal-plastic deformation of zircon: A defect in the assumption of chemical robustness. *Geology*, *34*(4), 257–260. https://doi.org/10.1130/G22110.1

Reddy, S. M., van Riessen, A., Saxey, D. W., Johnson, T. E., Rickard, W. D. A., Fougerouse, D., Fischer, S., Prosa, T. J., Rice, K. P., Reinhard, D. A., Chen, Y., & Olson, D. (2016). Mechanisms of deformation-induced trace element migration in zircon resolved by atom probe and correlative microscopy. *Geochimica et Cosmochimica Acta*, *195*, 158–170. https://doi.org/10.1016/j.gca.2016.09.019

Reddy, S. M., Wheeler, J., Butler, R. W. H., Cliff, R. A., Freeman, S., Inger, S., Pickles, C., & Kelley, S. P. (2003). Kinematic reworking and exhumation within the convergent Alpine Orogen. *Tectonophysics*, *365*(1–4), 77–102.

Reddy, S., Wheeler, J., & Cliff, R. (1999). The geometry and timing of orogenic extension: An example from the Western Italian Alps. *Journal of Metamorphic Geology*, *17*, 573–590. https://doi.org/10.1046/j.1525-1314.1999.00220.x

Reinecke, T. (1998). Prograde high-to ultrahigh-pressure metamorphism and exhumation of oceanic sediments at Lago di Cignana, Zermatt-Saas Zone, western Alps. *Lithos*, *42*(3–4), 147–189. https://doi.org/10.1016/S0024-4937(97)00041-8

Rickard, W. D., Reddy, S. M., Saxey, D. W., Fougerouse, D., Timms, N. E., Daly, L., Peterman, E., Cavosie, A. J., & Jourdan, F. (2020). Novel applications of FIB-SEM-based ToF-

SIMS in atom probe tomography workflows. *Microscopy and Microanalysis*, *26*, 1–8. https://doi.org/10.1017/S1431927620000136

Rocholl, A. B., Simon, K., Jochum, K. P., Bruhn, F., Gehann, R., Kramar, U., Luecke, W., Molzahn, M., Pernicka, E., Seufert, M., Spettel, B., & Stummeier, J. (1997). Chemical characterisation of NIST silicate glass certified reference material SRM 610 by ICP-MS, TIMS, LIMS, SSMS, INAA, AAS and PIXE. *Geostandards Newsletter*, *21*(1), 101–114. https://doi.org/10.1111/j.1751-908X.1997.tb00537.x

Rubatto, D., Gebauer, D., & Fanning, M. (1998). Jurassic formation and Eocene subduction of the Zermatt-Saas-Fee ophiolites: Implications for the geodynamic evolution of the Central and Western Alps. *Contributions to Mineralogy and Petrology*, *132*(3), 269–287. https://doi.org/10.1007/s004100050421

Sasaki, J., Peterson, N. L., & Hoshino, K. (1985). Tracer impurity diffusion in single-crystal rutile (TiO2− x). *Journal of Physics and Chemistry of Solids*, *46*(11), 1267–1283.

Saxey, D., Moser, D., Piazolo, S., Reddy, S., & Valley, J. (2018). Atomic worlds: Current state and future of atom probe tomography in geoscience. *Scripta Materialia*, *148*, 115–121. https://doi.org/10.1016/j.scriptamat.2017.11.014

Seydoux-Guillaume, A.-M., Fougerouse, D., Laurent, A., Gardés, E., Reddy, S., & Saxey, D. (2019). Nanoscale resetting of the Th/Pb system in an isotopically-closed monazite grain: A combined atom probe and transmission electron microscopy study. *Geoscience Frontiers*, *10*(1), 65–76. https://doi.org/10.1016/j.gsf.2018.09.004

Shannon, R. D. (1976). Revised effective ionic radii and systematic studies of interatomic distances in halides and chalcogenides. *Acta Crystallographica Section A: Crystal Physics, Diffraction, Theoretical and General Crystallography*, *32*(5), 751–767. https://doi.org/10.1107/S0567739476001551

Sills, R., & Cai, W. (2018). Free energy change of a dislocation due to a Cottrell atmosphere. *Philosophical Magazine*, *98*(16), 1491–1510. https://doi.org/10.1080/14786435.2018.1441560

Skora, S., Mahlen, N., Johnson, C. M., Baumgartner, L. P., Lapen, T., Beard, B. L., & Szilvagyi, E. (2015). Evidence for protracted prograde metamorphism followed by rapid exhumation of the Zermatt-Saas Fee ophiolite. *Journal of Metamorphic Geology*, *33*(7), 711–734. https://doi.org/10.1111/jmg.12148

Smye, A. J., & Stockli, D. F. (2014). Rutile U-Pb age depth profiling: A continuous record of lithospheric thermal evolution. *Earth and Planetary Science Letters*, *408*, 171–182. https://doi.org/10.1016/j.epsl.2014.10.013

Sutton, A. P., Balluffi, R. W., & Sutton, A. (1995). Interfaces in crystalline materials.

Swope, R. J., Smyth, J. R., & Larson, A. C. (1995). H in rutile-type compounds: I. Single-crystal neutron and X-ray diffraction study of H in rutile. *American Mineralogist*, *80*(5–6), 448–453. https://doi.org/10.2138/am-1995-5-604

Timms, N. E., Kinny, P. D., & Reddy, S. M. (2006). Enhanced diffusion of uranium and thorium linked to crystal plasticity in zircon. *Geochemical Transactions*, *7*(1), 10. https://doi.org/10.1186/1467-4866-7-10

Timms, N. E., Kinny, P. D., Reddy, S. M., Evans, K., Clark, C., & Healy, D. (2011). Relationship among titanium, rare earth elements, U–Pb ages and deformation microstructures in zircon: Implications for Ti-in-zircon thermometry. *Chemical Geology*, *280*(1–2), 33–46. https://doi.org/10.1016/j.chemgeo.2010.10.005

Tomkins, H. S., Powell, R., & Ellis, D. J. (2007). The pressure dependence of the zirconium-in-rutile thermometer. *Journal of Metamorphic Geology*, *25*(6), 703–713. https://doi.org/10.1111/j.1525-1314.2007.00724.x

Valley, J. W., Cavosie, A. J., Ushikubo, T., Reinhard, D. A., Lawrence, D. F., Larson, D. J., Clifton, P. H., Kelly, T. F., Wilde, S. A., Moser, D. E., & Spicuzza, M. J. (2014). Hadean age for a post-magma-ocean zircon confirmed by atom-probe tomography. *Nature Geoscience*, *7*(3), 219–223. https://doi.org/10.1038/ngeo2075

Valley, J. W., Reinhard, D. A., Cavosie, A. J., Ushikubo, T., Lawrence, D. F., Larson, D. J., Kelly, T. F., Snoeyenbos, D. R., & Strickland, A. (2015). Nano- and micro-geochronology in hadean and Archean zircons by atom-probe tomography and SIMS: New tools for old minerals. *American Mineralogist*, *100*(7), 1355–1377. https://doi.org/10.2138/am-2015-5134

van Actherbergh, E. (2001). Data reduction software for LA-ICP-MS. *Laser Ablation-ICP-Mass Spectrometry in the Earth Sciences: Principles and Applications*, 239–243.

van der Klauw, S., Reinecke, T., & Stöckhert, B. (1997). Exhumation of ultrahigh-pressure metamorphic oceanic crust from Lago di Cignana, Piemontese zone, western Alps: The structural record in metabasites. *Lithos*, *41*(1–3), 79–102. https://doi.org/10.1016/S0024-4937(97)82006-3

van Schrojenstein Lantman, H. W., Scambelluri, M., Gilio, M., Wallis, D., & Alvaro, M. (2021). Extensive fluid–rock interaction and pressure solution in a UHP fluid pathway recorded by garnetite, Lago di Cignana, Western Alps. *Journal of Metamorphic Geology*, *39*(4), 501–518.

Verberne, R., Reddy, S., Saxey, D., Fougerouse, D., Rickard, W., Plavsa, D., Agangi, A., & Kylander-Clark, A. (2020). The geochemical and geochronological implications of nanoscale trace-element clusters in rutile. *Geology*, *48*, 1126–1130. https://doi.org/10.1130/G48017.1

Verberne, R., Reddy, S. M., Saxey, D. W., Fougerouse, D., Rickard, W. D., Quadir, Z., & Clark, C. (2022). Dislocations in minerals: Fast-diffusion pathways or trace-element traps? *Earth and Planetary Science Letters*, *584*, 117517. https://doi.org/10.1016/j.epsl.2022.117517

Verberne, R., Saxey, D. W., Reddy, S. M., Rickard, W. D., Fougerouse, D., & Clark, C. (2019). Analysis of natural rutile (TiO2) by laser-assisted atom probe tomography. *Microscopy and Microanalysis*, *25*, 1–8. https://doi.org/10.1017/S1431927618015477

Vukmanovic, Z., Reddy, S. M., Godel, B., Barnes, S. J., Fiorentini, M. L., Barnes, S. J., & Kilburn, M. R. (2014). Relationship between microstructures and grain-scale trace element distribution in komatiite-hosted magmatic sulphide ores. *Lithos*, *184*, 42–61. https://doi.org/10.1016/j.lithos.2013.10.037

Vurpillot, F., Bostel, A., & Blavette, D. (2000). Trajectory overlaps and local magnification in three-dimensional atom probe. *Applied Physics Letters*, *76*(21), 3127–3129. https://doi.org/10.1063/1.126545

Watson, E. B., Wark, D. A., & Thomas, J. B. (2006). Crystallization thermometers for zircon and rutile. *Contributions to*

Mineralogy and Petrology, *151*(4), 413–433. https://doi.org/10.1007/s00410-006-0068-5

Whitney, D. L., & Evans, B. W. (2010). Abbreviations for names of rock-forming minerals. *American Mineralogist*, *95*, 185–197. https://doi.org/10.2138/am.2010.3371

Withers, A. C., Essene, E. J., & Zhang, Y. X. (2003). Rutile/TiO2II phase equilibria. *Contributions to Mineralogy and Petrology*, *145*(2), 199–204. https://doi.org/10.1007/s00410-003-0445-2

Zack, T., & Kooijman, E. (2017). Petrology and geochronology of rutile. *Reviews in Mineralogy and Geochemistry*, *83*(1), 443–467. https://doi.org/10.2138/rmg.2017.83.14

Zack, T., Kronz, A., Foley, S. F., & Rivers, T. (2002). Trace element abundances in rutiles from eclogites and associated garnet mica schists. *Chemical Geology*, *184*(1–2), 97–122. https://doi.org/10.1016/S0009-2541(01)00357-6

Zack, T., & Luvizottow, G. (2006). Application of rutile thermometry to eclogites. *Mineralogy and Petrology*, *88*(1–2), 69–85. https://doi.org/10.1007/s00710-006-0145-5

Zack, T., Moraes, R., & Kronz, A. (2004). Temperature dependence of Zr in rutile: Empirical calibration of a rutile thermometer. *Contributions to Mineralogy and Petrology*, *148*(4), 471–488. https://doi.org/10.1007/s00410-004-0617-8

Zack, T., von Eynatten, H., & Kronz, A. (2004). Rutile geochemistry and its potential use in quantitative provenance studies. *Sedimentary Geology*, *171*(1–4), 37–58. https://doi.org/10.1016/j.sedgeo.2004.05.009

Zhou, T., Li, Q., Klemd, R., Shi, Y., Tang, X., Li, C., & Liu, Y. (2020). Multi-system geochronology in North Dabie eclogite: Ineffective garnet 'shielding' on rutile inclusions under multi-thermal conditions. *Lithos*, *368*, 105573. https://doi.org/10.1016/j.lithos.2020.105573

SUPPORTING INFORMATION

Additional supporting information can be found online in the Supporting Information section at the end of this article.

Data S1. (DR-1) **Matlab scripts:** The matlab scripts used for EBSD and TKD analysis

Data S2. APT acquisition conditions: overview of data acquisition and reconstruction parameters for atom probe tomography as recommended by Blum et al., (2018)

Data S3. (DR-3) **LA-ICP-MS Data:** Complete table of LA-ICP-MS spot measurements

Video S1. (DR-4) **3D APT Specimens:** 3D animation to show the nanoscale structures within the two APT datasets analysed.

Video S2. (DR-5)Animation to show the difference in concentration between the two branches in specimen M2

Data S4. (DR-6) 3D models for specimen M2 and M5 to show the distribution of trace elements (Al, Si, Fe, OH, H, Zr and Ca). Use the scroll wheel to zoom in/out, hold right mouse button to drag the model, hold left mouse button to rotate the specimen.

Figure S1. (DR-7) Microphotograph of the thick section used for LA-ICP-MS measurements and Zr-in-rutile thermometry

How to cite this article: Verberne, R., van Schrojenstein Lantman, H. W., Reddy, S. M., Alvaro, M., Wallis, D., Fougerouse, D., Langone, A., Saxey, D. W., & Rickard, W. D. A. (2022). Trace-element heterogeneity in rutile linked to dislocation structures: Implications for Zr-in-rutile geothermometry. *Journal of Metamorphic Geology*, 1–22. https://doi.org/10.1111/jmg.12686